



# NAVAL POSTGRADUATE SCHOOL

MONTEREY, CALIFORNIA

## THESIS

**DIFFUSION COUPLE ALLOYING OF REFRactory  
METALS IN AUSTENITIC AND  
FERRITIC/MARTENSITIC STEELS**

by

Alexander L. McGinnis

March 2012

Thesis Advisor:

Second Reader:

Luke Brewer

Sarath Menon

**Approved for public release; distribution is unlimited**

THIS PAGE INTENTIONALLY LEFT BLANK

**REPORT DOCUMENTATION PAGE**
*Form Approved OMB No. 0704-0188*

Public reporting burden for this collection of information is estimated to average 1 hour per response, including the time for reviewing instruction, searching existing data sources, gathering and maintaining the data needed, and completing and reviewing the collection of information. Send comments regarding this burden estimate or any other aspect of this collection of information, including suggestions for reducing this burden, to Washington Headquarters Services, Directorate for Information Operations and Reports, 1215 Jefferson Davis Highway, Suite 1204, Arlington, VA 22202-4302, and to the Office of Management and Budget, Paperwork Reduction Project (0704-0188) Washington DC 20503.

<b>1. AGENCY USE ONLY (Leave blank)</b>	<b>2. REPORT DATE</b> March 2012	<b>3. REPORT TYPE AND DATES COVERED</b> Master's Thesis
<b>4. TITLE AND SUBTITLE</b> Diffusion Couple Alloying of Refractory Metals in Austenitic and Ferritic/Martensitic Steels		<b>5. FUNDING NUMBERS</b>
<b>6. AUTHOR(S)</b> Alexander L. McGinnis		
<b>7. PERFORMING ORGANIZATION NAME(S) AND ADDRESS(ES)</b> Naval Postgraduate School Monterey, CA 93943-5000		<b>8. PERFORMING ORGANIZATION REPORT NUMBER</b>
<b>9. SPONSORING /MONITORING AGENCY NAME(S) AND ADDRESS(ES)</b> N/A		<b>10. SPONSORING/MONITORING AGENCY REPORT NUMBER</b>
<b>11. SUPPLEMENTARY NOTES</b> The views expressed in this thesis are those of the author and do not reflect the official policy or position of the Department of Defense or the U.S. Government. IRB Protocol number _____ n/a_____.		
<b>12a. DISTRIBUTION / AVAILABILITY STATEMENT</b> Approved for public release; distribution is unlimited		<b>12b. DISTRIBUTION CODE</b>
<b>13. ABSTRACT (maximum 200 words)</b>		
<p>This thesis utilized the diffusion couple approach to evaluate the addition of molybdenum, niobium, tantalum, and tungsten to 316 stainless (316SS) and alloy HT9 steels. Refractory elements have been previously studied as alloying candidates to mitigate problems such as radiation-induced segregation, void swelling, and irradiation creep in reactor steels. Diffusion couples were characterized via energy dispersive x-ray spectroscopy (EDS) and nanoindentation to examine refractory element solubility, diffusivity, and the effects these elements have on hardness and elastic modulus in 316SS and alloy HT9. Molybdenum and tungsten samples showed significantly higher solubility and diffusivity than niobium and tantalum, with evidence of multiphase regions several hundred microns from the diffusion couple interface. Nanoindentation revealed evidence of hardening as a function of increasing concentration for some, but not all of the refractory elements. Diffusion of the refractory elements in alloy HT9 was significantly higher than in 316SS, which suggests that alloy HT9 retained its ferritic structure even at high temperatures, i.e., 1100°C.</p>		

<b>14. SUBJECT TERMS</b> Refractory elements, diffusion couple, nuclear, alloy 316SS, alloy HT9, Mo, Nb, Ta, W		<b>15. NUMBER OF PAGES</b> 95	
<b>16. PRICE CODE</b>			
<b>17. SECURITY CLASSIFICATION OF REPORT</b> Unclassified	<b>18. SECURITY CLASSIFICATION OF THIS PAGE</b> Unclassified	<b>19. SECURITY CLASSIFICATION OF ABSTRACT</b> Unclassified	<b>20. LIMITATION OF ABSTRACT</b> UU

THIS PAGE INTENTIONALLY LEFT BLANK

**Approved for public release; distribution is unlimited**

**DIFFUSION COUPLE ALLOYING OF REFRactory METALS  
IN AUSTENITIC AND FERRITIC/MARTENSITIC STEELS**

Alexander L. McGinnis  
Lieutenant, United States Navy  
B.S., Oregon State University, 2005

Submitted in partial fulfillment of the  
requirements for the degree of

**MASTER OF SCIENCE IN MECHANICAL ENGINEERING**

from the

**NAVAL POSTGRADUATE SCHOOL  
March 2012**

Author: Alexander L. McGinnis

Approved by: Luke N. Brewer  
Thesis Advisor

Sarath Menon  
Second Reader

Knox T. Millsaps  
Chair, Department of Mechanical and Aerospace Engineering

THIS PAGE INTENTIONALLY LEFT BLANK

## ABSTRACT

This thesis utilized the diffusion couple approach to evaluate the addition of molybdenum, niobium, tantalum, and tungsten to 316 stainless (316SS) and alloy HT9 steels. Refractory elements have been previously studied as alloying candidates to mitigate problems such as radiation-induced segregation, void swelling, and irradiation creep in reactor steels. Diffusion couples were characterized via energy dispersive x-ray spectroscopy (EDS) and nanoindentation to examine refractory element solubility, diffusivity, and the effects these elements have on hardness and elastic modulus in 316SS and alloy HT9. Molybdenum and tungsten samples showed significantly higher solubility and diffusivity than niobium and tantalum, with evidence of multiphase regions several hundred microns from the diffusion couple interface. Nanoindentation revealed evidence of hardening as a function of increasing concentration for some, but not all of the refractory elements. Diffusion of the refractory elements in alloy HT9 was significantly higher than in 316SS, which suggests that alloy HT9 retained its ferritic structure even at high temperatures, i.e., 1100°C.

THIS PAGE INTENTIONALLY LEFT BLANK

## TABLE OF CONTENTS

I.	INTRODUCTION.....	1
A.	MOTIVATION: ALLOY DEVELOPMENT FOR ADVANCED NUCLEAR ENERGY APPLICATIONS .....	1
B.	REVIEW OF DAMAGE MECHANISMS FOR NUCLEAR REACTOR STEELS .....	2
1.	Basic Theory of Neutron Irradiation Damage .....	2
a.	<i>Radiation Hardening</i> .....	3
b.	<i>Irradiation-Induced Precipitation and Grain Boundary Segregation</i> .....	4
c.	<i>Swelling and Void Formation</i> .....	8
d.	<i>Embrittlement and Loss of Fracture Toughness</i> .....	10
e.	<i>Irradiation Creep</i> .....	11
2.	Design Considerations for Materials in Nuclear Applications .....	11
3.	Alloy 316 Stainless Steel and its Application in Nuclear Engineering.....	12
4.	Alloy HT9 Ferritic/Martensitic Steel and its Application in Nuclear Engineering .....	17
C.	SOLID SOLUTION MODIFICATION FOR IMPROVED REACTOR STEEL PERFORMANCE .....	20
1.	Addition of Oversized Solutes to Mitigate RIS in Austenitic Stainless Steel .....	22
2.	Evolution of Ferritic/Martensitic Steel for Reduced Activation and Higher Creep-Rupture Strength in Nuclear Applications.....	22
D.	DIFFUSION COUPLE AND MULTIPLE APROACHES: A HIGH THROUGHPUT METHOD FOR RAPID ALLOY DEVELOPMENT...24	
E.	THESIS QUESTIONS.....	25
1.	What is the Maximum Amount of Refractory Element that can be Added in Each Alloy before the Solubility Limit is Reached? .....	26
2.	What is the Relative Diffusivity for Each Refractory Element in Alloy 316 and Alloy HT9? .....	27
3.	What is the Change in Hardness, Yield Stress, and Young's Modulus with the Addition of the Refractory Element? .....	27
4.	Is the Diffusion Couple Approach a Useful Tool in Reactor Steel Development? .....	28
II.	METHODS .....	29
A.	DIFFUSION COUPLE FABRICATION .....	29
B.	MATERIAL CHARACTERIZATION .....	31
1.	Equipment .....	31
2.	Assumptions.....	31
3.	Experimental Procedure and Parameters .....	33

a.	<i>Obtaining X-ray Spectrum of the Standards and Specimen under Defined and Reproducible Conditions .....</i>	33
b.	<i>Measuring Standards Containing the Elements that have been Identified in the Specimen .....</i>	34
c.	<i>Processing the Spectra of the Standards and Specimen to Remove the Background from the X-ray Peaks, so that the Measured Intensities Consist only of the Characteristic Signal.....</i>	35
d.	<i>Developing the X-ray Intensity Ratios using the Specimen Intensity <math>I_i</math> and the Standard Intensity <math>I_{(i)}</math> for Each Element Present in the Sample and Carrying out Matrix Corrections to Obtain Quantitative Concentration Values.....</i>	36
4.	<b>Calculation of “Effective” Diffusion Constants .....</b>	37
C.	<b>NANOINDENTATION .....</b>	39
1.	<b>Equipment .....</b>	39
2.	<b>Assumptions.....</b>	40
3.	<b>Experimental Procedure and Parameters .....</b>	42
III.	<b>RESULTS AND DISCUSSION .....</b>	45
A.	<b>OPTICAL MICROSCOPY.....</b>	45
B.	<b>MATERIAL CHARACTERIZATION .....</b>	48
1.	<b>Refractory Element Composition versus Position .....</b>	48
2.	<b>“Effective” Diffusion Constants.....</b>	51
3.	<b>Nanoindentation.....</b>	51
C.	<b>DISCUSSION: THESIS QUESTION REVISITATION.....</b>	55
1.	<b>What is the Maximum Amount of Refractory Element that can be Added in Each Alloy before the Solubility Limit is Reached? .....</b>	55
2.	<b>What is the Relative Diffusivity for Each Refractory Element in Alloy 316 and Alloy HT9? .....</b>	61
3.	<b>What is the Change in Hardness, Yield Stress, and Young’s Modulus with the Addition of the Refractory Element? .....</b>	62
4.	<b>Is the Diffusion Couple Approach a Useful Tool in Reactor Steel Development? .....</b>	66
D.	<b>FUTURE WORK .....</b>	67
IV.	<b>CONCLUSIONS .....</b>	69
<b>LIST OF REFERENCES .....</b>		71
<b>INITIAL DISTRIBUTION LIST .....</b>		75

## LIST OF FIGURES

Figure 1.	Tensile deformation of polycrystalline Fe: (a) proton irradiated; (b) neutron irradiated. Annotation on each tensile deformation curve represents displacements per atom (dpa) (From [8]).	4
Figure 2.	Typical segregation profiles in commercial-purity Type 304 stainless steel neutron-irradiated to $\sim 10^{22}$ n/cm <sup>2</sup> at 275 °C (From [9])	6
Figure 3.	Neutron fluence effects on IASCC susceptibility of Type 304 stainless steel in BWR environments (From [1]).	7
Figure 4.	Dependence of RIS on homologous temperature and dose rate for austenitic stainless steels (From [1]).	8
Figure 5.	Microstructure of SA Type 304 SS fuel subassembly hex can irradiated in EBR-II at 370 °C to 50 dpa; (a) voids near grain boundary, (b) high magnification, (c) voids and twins in low magnification, and (d) dark-field image of dense carbide precipitates. (From [10])	9
Figure 6.	Charpy impact curves for Sandvik HT9 (12Cr-1MoVW) in the unirradiated condition and after irradiation to 10 and 17 dpa at 365 °C in Fast Flux Test Facility (From [12]).	10
Figure 7.	Schematic diagram of core internals of a PWR indicating typical material and end-of-life displacement dose ranges (From [3]).	14
Figure 8.	a) PFR standard core subassembly. b) Fast reactor core fuel element subassembly bowing, dilation, and length increase resulting from irradiation (From [16]).	16
Figure 9.	Swelling behavior of six commercial heats of ferritic/martensitic steels compared to type 316 stainless steel after irradiation in Experimental Breeder Reactor-II at 420 °C to $\sim 80$ dpa (From [7]).	18
Figure 10.	Key components of the tokomak fusion reactor: 1 – central solenoid; 2 – shield/blanket; 3 – plasma; 4 – vacuum vessel shield; 5 – plasma exhaust; 6 – cryostat; 7 – active coil; 8 – toroidal field coils; 9 – first wall; 10 – divertor plates; 11 – poloidal field coils (From [3]).	20
Figure 11.	A comparison of 100000 h rupture strengths for Sandvik HT9, EUROFER, F82H, modified 9Cr-1Mo, and NF616 at 550, 600, and 650 °C (From [12]).	23
Figure 12.	Flow diagram of informatic processes utilized in the diffusion multiple approach (From [21]).	25
Figure 13.	(a) optical image of a Nb-Ti-Si-Cr diffusion multiple; (b) EPMA Cr map of the Cr-Ti binary diffusion couple region showing the formation of Laves phases (Cr <sub>2</sub> Ti) and precipitation of the C-15 Laves phas from bcc(Ti,Cr) during sample cooling from 1100°C to room temperature (From [21]).	27
Figure 14.	(Top) Photograph of diffusion couple block after hot isostatic pressing. (Bottom) Schematic of diffusion couple cylinders.	30
Figure 15.	Diffusion couple coupon after sectioning and polishing as received from Sandia National Laboratories.	30

Figure 16.	Visual representation of the assumption of 1-D diffusion on solute refractory element composition, Nb/316SS diffusion couple, optical image.....	32
Figure 17.	SEM Image of Mo/HT9 diffusion couple interface showing the intermetallic and multi-phase regions.....	32
Figure 18.	Geller pure standards block with associated element/compound map. ....	34
Figure 19.	EDS spectrum for FeS <sub>2</sub> pure standard. ....	35
Figure 20.	EDS spectrum for FeS <sub>2</sub> pure standard with background subtracted. ....	36
Figure 21.	Log plot of concentration C(x,t) versus x <sup>2</sup> for Mo/HT9 sample.....	39
Figure 22.	(Top) Agilent G200 Nanoindenter. (Bottom) Indenter column schematic (From [24]).....	40
Figure 23.	3 x n indentation sequence for the Ta/316SS diffusion couple. ....	41
Figure 24.	Plot of modulus vs. indentation depth for 3 indentations, Mo/316SS sample. ....	42
Figure 25.	Optical microscopy images of 316SS diffusion couple specimens. Top left: molybdenum; top right: niobium; bottom left: tantalum; bottom right: tungsten. All images are oriented with the refractory element on the left side and base metal on the right.....	45
Figure 26.	Optical microscopy images of HT9 diffusion couple specimens. Top left: molybdenum; top right: tantalum; bottom left: tungsten. All images are oriented with the refractory element on the left side and base metal on the right. ....	46
Figure 27.	(Top) Optical image of Mo/HT9 sample showing inter-metallic phase formations; (Bottom) SEM image of Mo/HT9 sample showing the extent of formation. ....	47
Figure 28.	Overlaid EDS spectra near and far away from the diffusion couple interface for Mo/316SS sample. ....	48
Figure 29.	Plots of weight percent versus position from interface for 316SS and HT9 diffusion couples.....	49
Figure 30.	SEM Image of multi-phase regions in (Top) Mo/HT9 sample, (Bottom) W/HT9 sample.....	50
Figure 31.	Plots of modulus and hardness vs. position from interface for 316SS diffusion couples.....	53
Figure 32.	Plots of modulus and hardness vs. position from interface for HT9 diffusion couples.....	55
Figure 33.	EDS overlay spectra for Ta/316 (top) and Ta/HT9 (bottom) diffusion couples .....	56
Figure 34.	Micrograph image of Ta/HT9 sample, showing evidence of microstructural change near the interface. ....	57
Figure 35.	Ternary phase diagram for Fe-Cr-Mo (top), and Fe-Cr-W (bottom) (isothermal sections at 1100 °C). The intersection of the 3 lines shows the approximate compositions measured near the interface for the alloy HT9 diffusion couples. Blue regions in the diagram represent $\alpha$ -ferrite phase, white regions represent dual-phase of ferrite/inter-metallic, and yellow	

regions are three-phase region of ferrite and two different inter-metallic phases (From [26]).....	59
Figure 36. Fe-Cr-Ni ternary phase diagram showing the thermodynamic state at max solubility for Mo/316 sample based on the Shaeffler-DeLong equivalent Cr. The blue region to the right of the ternary diagram is $\gamma$ -Fe phase (From [26]).....	60
Figure 37. Graphs of modulus and hardness as a function of weight percent refractory elements in alloy 316SS. Lines added to aid the eye in trends. ....	63
Figure 38. Graphs of modulus and hardness as a function of weight percent refractory elements in alloy HT9. Lines added to aid the eye in trends. ....	64

THIS PAGE INTENTIONALLY LEFT BLANK

## LIST OF TABLES

Table 1.	Typical thermodynamic and fuel characteristics for six reference power reactor types: boiling water reactor(BWR), pressured water reactor(PWR), pressurized heavy water reactor (PHWR), high-temperature gas reactor(HTGR), advanced gas-cooled reactor(AGR), and liquid metal fast breeder reactor(LMFBR) (From [13]). .....	12
Table 2.	Nominal composition of Alloy 316 including the function of each alloying element (From [14]).....	13
Table 3.	Nominal composition of Alloy HT9 including the function of each alloying element (From[12], [14]) .....	17
Table 4.	Atomic radii and percent mismatch of each refractory element in relation to the atomic radius of iron. Included in this table are values of other alloying candidates for addition to steel to mitigate adverse effects of neutron irradiation. (Atomic radii values From [17]) .....	21
Table 5.	Diffusion Couples Available for Analysis .....	26
Table 6.	SEM Parameters used in pure standards and experimental EDS .....	33
Table 7.	Pure standards used for quantitative analysis. ....	34
Table 8.	Calculated Pure Element Intensities ( $I_{(i)}$ ).....	36
Table 9.	EDS Specimen sample ranges for each diffusion couple .....	37
Table 10.	CSM method nanoindentation parameters.....	43
Table 11.	Composition (in wt%) of dual-phase formations in Mo/HT9 sample. ....	51
Table 12.	Calculated “Effective” diffusivity for refractory elements into their respective alloys.....	51
Table 13.	Comparison of experimentally-determined diffusivities with those measured in previous works.....	61
Table 14.	List of absolute changes in hardness, Young’s Modulus, and estimated change in yield stress. ....	65

THIS PAGE INTENTIONALLY LEFT BLANK

## LIST OF ACRONYMS AND ABBREVIATIONS

AGR	Advanced Gas Reactor
BCC	Body-centered Cubic
CSM	Continuous Stiffness Measurement
DBTT	Ductile-to-brittle Transition Temperature
Dpa	Displacements per Atom
EBSD	Electron Backscatter Diffractometry
EDM	Electro-discharge Machining
EDS	Energy-dispersive Spectroscopy
EOL	End-of-Life
FCC	Face-centered Cubic
FIB	Focused Ion Beam
HTGR	High Temperature Gas Reactor
IASCC	Irradiation-assisted Stress Corrosion Cracking
LMFBR	Liquid Metal Fast Breeder Reactor
NPS	Naval Postgraduate School
PHWR	Pressurized Heavy Water Reactor
PKA	Primary Knock-on Atom
PWR	Pressurized Water Reactor
RIS	Radiation-induced Segregation
SDD	Silicon Drift Detector
TCP	Topologically Close-packed
TEM	Transmission Electron Microscope

THIS PAGE INTENTIONALLY LEFT BLANK

## ACKNOWLEDGMENTS

First and foremost, I would like to thank Professor Luke Brewer for his patience, guidance, constructive criticism, and expertise through my time at Naval Postgraduate School. He is truly an asset to the field of material science, and I consider myself enlightened after having been his student.

Secondly, I would like to thank Professor Sarah Menon. He went to great lengths to help me in accomplishing this work, whether it was hands-on assistance in the lab, finding literature where I thought not to look, or providing moral support and guidance to help keep my eyes on the prize.

This work would have not been possible without the gracious collaboration with Khalid Hattar at Sandia National Laboratories in Albuquerque, New Mexico to provide the material for this study. Thank you.

Lastly, to my loving and understanding wife, Sarah: thank you for enduring my irritability during the past two years and providing a pillar in which to lean upon. I am truly blessed to have you by my side.

THIS PAGE INTENTIONALLY LEFT BLANK

## I. INTRODUCTION

### A. MOTIVATION: ALLOY DEVELOPMENT FOR ADVANCED NUCLEAR ENERGY APPLICATIONS

Since the early 1950s, nuclear energy has grown to become an important alternative to coal and fossil fuels for commercial power generation. Nuclear energy now comprises approximately 17% of the world's power production [1]. The growing concern over depletion of fossil fuels has spurred the push for new technologies in the nuclear industry; additionally, the need has arisen to extend the operational lifetime of existing nuclear power facilities.

Steels are widely used in pressurized water (thermal) reactors (PWR), boiling water reactors (BWR), and liquid metal fast breeder reactors (LMFBR) for their strength at high temperature, good ductility, general corrosion resistance, and relatively moderate cost. The applications of austenitic stainless steel and ferritic/martensitic steel can vary from structural and support components in the reactor core to reactor fuel cladding depending on the type of reactor plant. Whether used in thermal or fast fission reactor plants, one fact is certain: the material will be exposed to large amounts of neutron irradiation (e.g., greater than 150 displacements per atom) at elevated temperatures (e.g., temperatures over 600°C) over a long period of time (e.g., several years).

The result of prolonged radiation can have serious consequences in regards to safe nuclear power plant operation as the resultant radiation damage can compromise the material's microstructure, affect geometry (in which critical clearances are required), or render plant components more susceptible to failure. These detrimental effects can be categorized into five broad categories [1], [2]:

1. Radiation hardening
2. Precipitation and grain boundary segregation
3. Swelling (void formation)
4. Embrittlement and loss of fracture toughness
5. Irradiation creep

Much study has been devoted to developing alloys that are resistant to these radiation-induced effects [3–6]. A variety of austenitic and ferritic/martensitic steels have been developed to mitigate these phenomena.

## **B. REVIEW OF DAMAGE MECHANISMS FOR NUCLEAR REACTOR STEELS**

### **1. Basic Theory of Neutron Irradiation Damage**

Fast neutrons resulting from the fission process are born at energy levels ranging from 1 to 2 MeV. By comparison, the energy of fast neutrons produced from fusion is 14.1 MeV. Whether produced by fission or fusion, these energies are much greater than the binding energy of the atoms in the material through which it passes. These large neutron energies guarantee that if a fast neutron strikes a lattice atom, displacement of that atom will occur. The displaced atom is referred to as a primary knock-on atom (PKA). Once freed of the lattice, the PKA has its own kinetic energy, and it goes on to produce secondary collisions, which may free those atoms as well. This process is known as a displacement cascade [2].

As the PKA and the secondary atoms move away from their previous positions, a cluster of vacancies is created in the lattice, which Olander refers to as a displacement zone, or depletion spike [2]. Fission fragments can also play a part in radiation damage, as they react in a similar fashion in displacing the atoms in the lattice. Finally, the fast neutron has the potential to transfer its energy until it reaches thermal energy ( $E < 0.2\text{MeV}$ ). These neutrons can no longer create displacements. However, if absorbed, thermal neutrons can cause a secondary decay, and the decay product atom can recoil to produce additional displacements in the lattice. It is important to note that reactor core materials, regardless of the neutron energy application (i.e., fast fission or thermal fission) will be subject to fast neutron energy damage since the vast majority of neutrons from fission are born at fast energies.

The vacancies and interstitials produced by these cascading events result in stacking faults in the lattice. These stacking faults then create a circular edge dislocation known as a Frank sessile dislocation loop as the surrounding planes of atoms collapse

around them. These dislocation loops are immobile, and the stacking fault can only be corrected by a dislocation moving through it. This process (referred to as unfaulting) will occur if the temperature is high enough to promote dislocation motion (approximately 600°C for stainless steels, for example) [2]. When the unfaulting process occurs, the burgers vector of these loops is changed to facilitate motion, and these loops (known as prismatic loops) can now move via slip. It is common to see these unfaulted loops lose their circular pattern as they move through a lattice and entangle with other mobile and/or sessile dislocations.

The physics behind these interactions is beyond the scope of this paper. However, it is important to understand the effect that bombarding neutrons, fission fragments, and the secondary particles have on the lattice of a material whether it be the fuel cladding, support structures, or any material exposed to a high neutron flux. A common method of quantifying displacement damage is in units of displacements per atom, or dpa [7]. Additionally, the damage done is a complex function of several variables. Dose, dose rate, and irradiation temperature are three such variables.

The effect of displacements caused by neutron irradiation can be characterized in the following detrimental phenomena:

#### *a. **Radiation Hardening***

The formation of vacancies and interstitials from irradiation leads to dislocation loop formation in steels. Additionally, these defects impede dislocation motion. Ultimately, as dislocation density rises in the material, so does its tensile strength and hardness. This is known as radiation hardening.

As an example, Victoria et al. performed tensile and hardness tests for a variety of FCC and BCC materials. They concluded that dislocation loop formation in all materials, with an associated rapid increase in yield stress, was proportional to irradiation dose. Figure 1 shows the resultant stress-strain curves for irradiated iron.

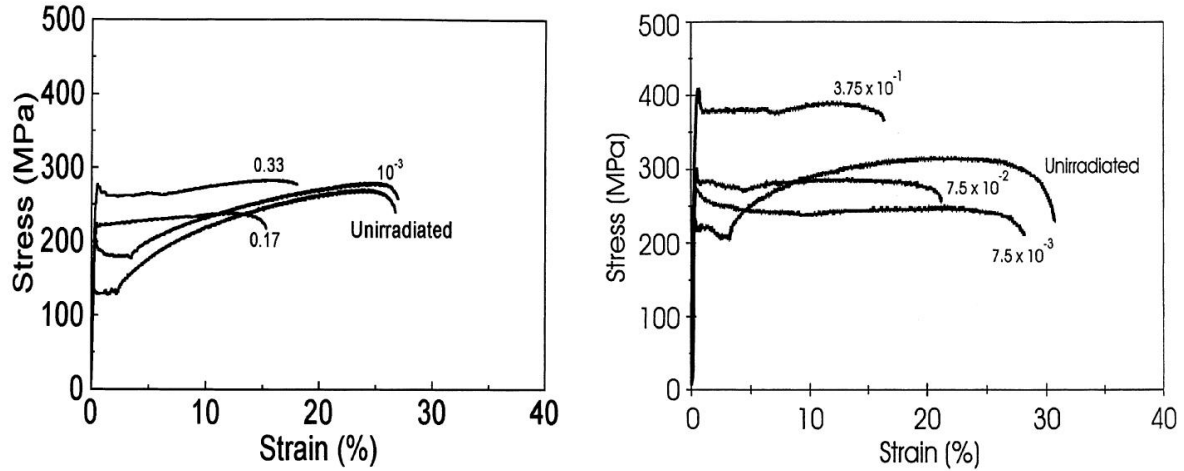


Figure 1. Tensile deformation of polycrystalline Fe: (a) proton irradiated; (b) neutron irradiated. Annotation on each tensile deformation curve represents displacements per atom (dpa) (From [8]).

Observations on irradiated austenitic steel determined that two deformation modes were present: dislocation channeling and deformation twinning. In dislocation channeling, moving dislocations sweep radiation defects in the slip plane, resulting in depleted defects in that plane. This effect clears the way for following dislocations, which then result in regions of localized, channel-like deformation. Twinning was shown to be particular to austenitic steel, where localized strain was observed at low temperatures; however once temperature was raised in the samples, the main mode was dislocation channeling [8].

#### *b. Irradiation-Induced Precipitation and Grain Boundary Segregation*

In materials with multiple elements such as steel, it is possible for radiation to cause precipitation of one or more phases at grain boundaries or in the matrix to occur. Neutron irradiation accelerates carbide precipitation reactions that otherwise would not occur at the relative operating temperatures of steel. In Alloy 316, carbide precipitation will occur with exposure to fluences between  $10^{21} - 10^{22}$  neutrons  $\text{cm}^{-2}$  and irradiation temperature between 400 – 900°C. Precipitation has also been observed in HT9 steel irradiated to  $\sim 5 \times 10^{25}$  neutrons  $\text{cm}^{-2}\text{sec}^{-1}$  [4]. Because of their brittle

characteristics, if precipitates form on the grain boundaries then mechanical properties of the steel such as strength and fracture toughness is adversely affected [2].

Another phenomenon resulting from irradiation of metals is radiation-induced segregation (RIS). Was defines RIS as the “redistribution of major alloying elements and the enrichment or depletion of impurity elements at point defect sinks” [1]. The driving factor for RIS is that of the movement of radiation defects (primarily vacancies) to sinks (i.e., grain boundaries, precipitates, and voids). In steels, oversized solutes such as molybdenum and chromium diffuse away from the grain boundaries, while undersized solutes such as silicon and phosphorus diffuse towards the grain boundaries. The result of all of this mass transfer is RIS, segregation of large atoms at grain boundaries and depletion of smaller atoms from grain boundaries (Figure 2). The size of the solute is not the sole factor in determining the direction of diffusion, however. The inverse Kirkendall effect is a phenomenon for which elements with high diffusivities exchange more frequently with radiation-induced vacancies than those with low diffusivities. This results in the depletion of fast-diffusing solutes (i.e., Cr) from grain boundaries while slow-diffusing solutes (i.e., Ni) enrich toward them.

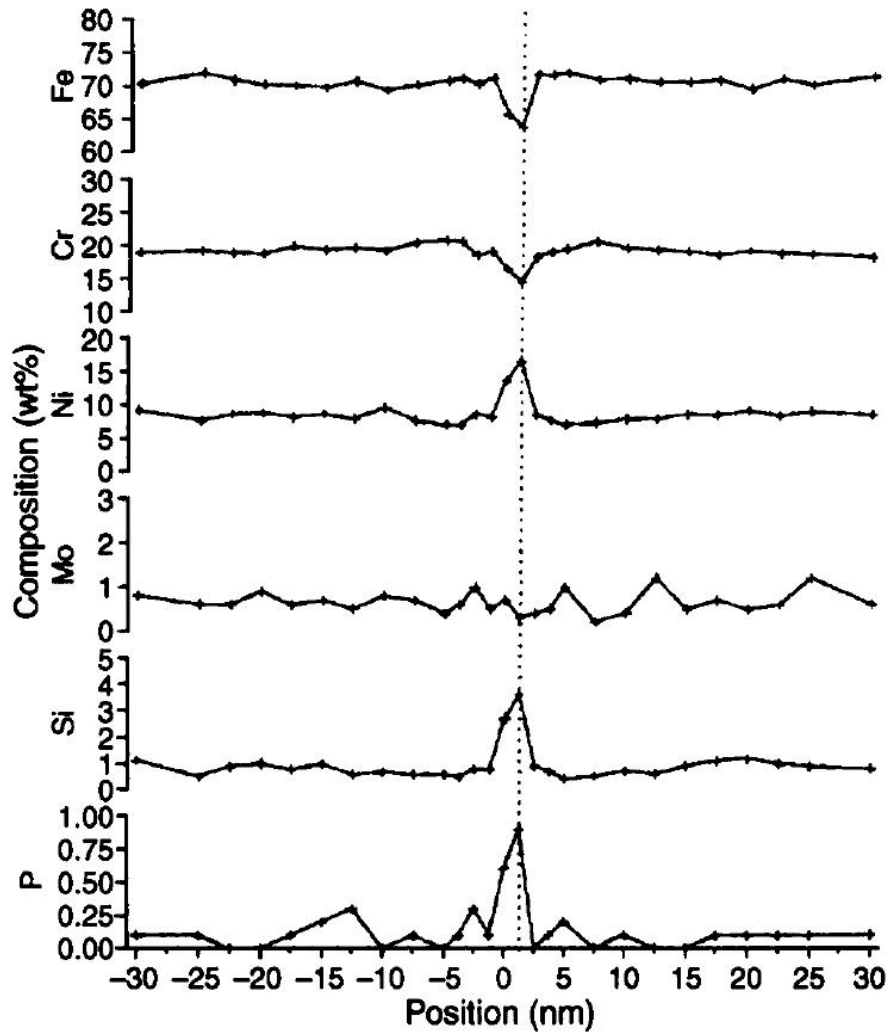


Figure 2. Typical segregation profiles in commercial-purity Type 304 stainless steel neutron-irradiated to  $\sim 10^{22}$  n/cm<sup>2</sup> at 275 °C (From [9])

RIS has serious implications in steel because the segregation of alloying elements can jeopardize structural integrity and compromise mechanical and corrosion properties. With sufficient RIS, the assumption that material properties such as modulus and yield strength are the same as a homogenous solid solution may no longer be accurate.

Austenitic stainless steel is particularly susceptible to irradiation-induced stress corrosion cracking (IASCC), a by-product of RIS. The phenomenon was first discovered in the 1960s, where time, neutron flux, and stress level were determined to

play a part in the failure of reactor plant components due to inter-granular (IG) cracking [1]. Figure 3 shows a relative timeline for common component failures in BWR systems.

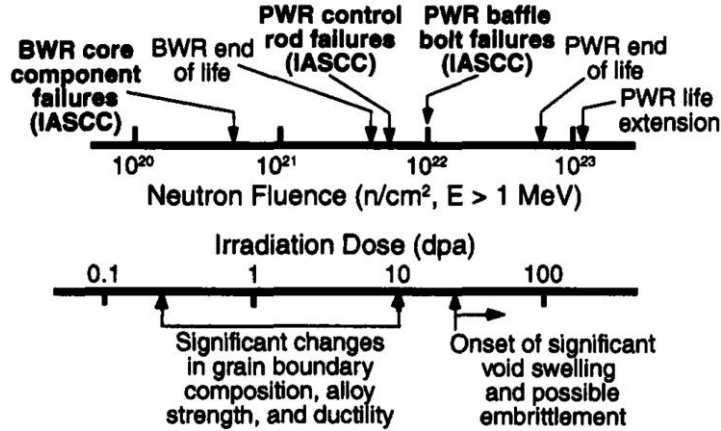


Figure 3. Neutron fluence effects on IASCC susceptibility of Type 304 stainless steel in BWR environments (From [1]).

The rate of radiation-induced segregation is strongly influenced by irradiation temperature, dose, and dose rate. At low temperatures, segregation is low due to lack of mobility. At sufficiently high irradiation temperatures, however, RIS is limited due to backward diffusion of segregants [1]. At low dose rates, RIS is higher than at high dose rates, since high dose rates produce a high enough level of defects to promote recombination (defects cancelling each other). The effect of relative ranges of irradiation temperature versus radiation flux with regard to RIS can be seen below.

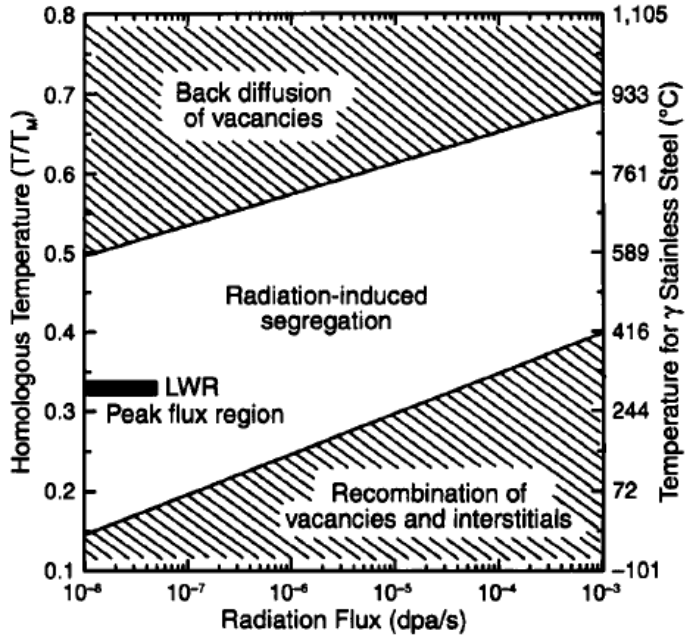


Figure 4. Dependence of RIS on homologous temperature and dose rate for austenitic stainless steels (From [1]).

The effect of RIS on the bulk material is the increased susceptibility to IG cracking. One hypothesis why this occurs is that the loss of Cr from the grain boundaries reduces the passive oxide-forming ability at that location, which makes the grain boundaries more susceptible to corrosion

### *c. Swelling and Void Formation*

As the nuclear power plants in operation today grow older, a pressing concern is the effect of void formation and the subsequent swelling (decrease in density) of materials subject to neutron flux, particularly toward the end of life (EOL).

Void formation is the result of radiation-induced vacancies diffusing toward sinks such as external surfaces, grain boundaries, or phase interfaces. If the radiation damage is sufficiently extensive (a report the NRC defines as fluence levels  $> 10^{23} \text{ n/cm}^2$ ,  $E > 0.1 \text{ MeV}$ ), then these voids can significantly affect mechanical properties and cause misfits in components (thereby causing an increase in residual stresses) [10]. Data from research of this phenomenon indicates that there is an incubation period, followed by formation of voids in a material. Once voids begin to form, a steady state

swelling rate of 1% per dpa is typically observed. Figure 5 illustrates void formation in austenitic steel after extended exposure to neutron flux (note the existence of twinning and formation of carbide precipitates as discussed earlier in this paper).

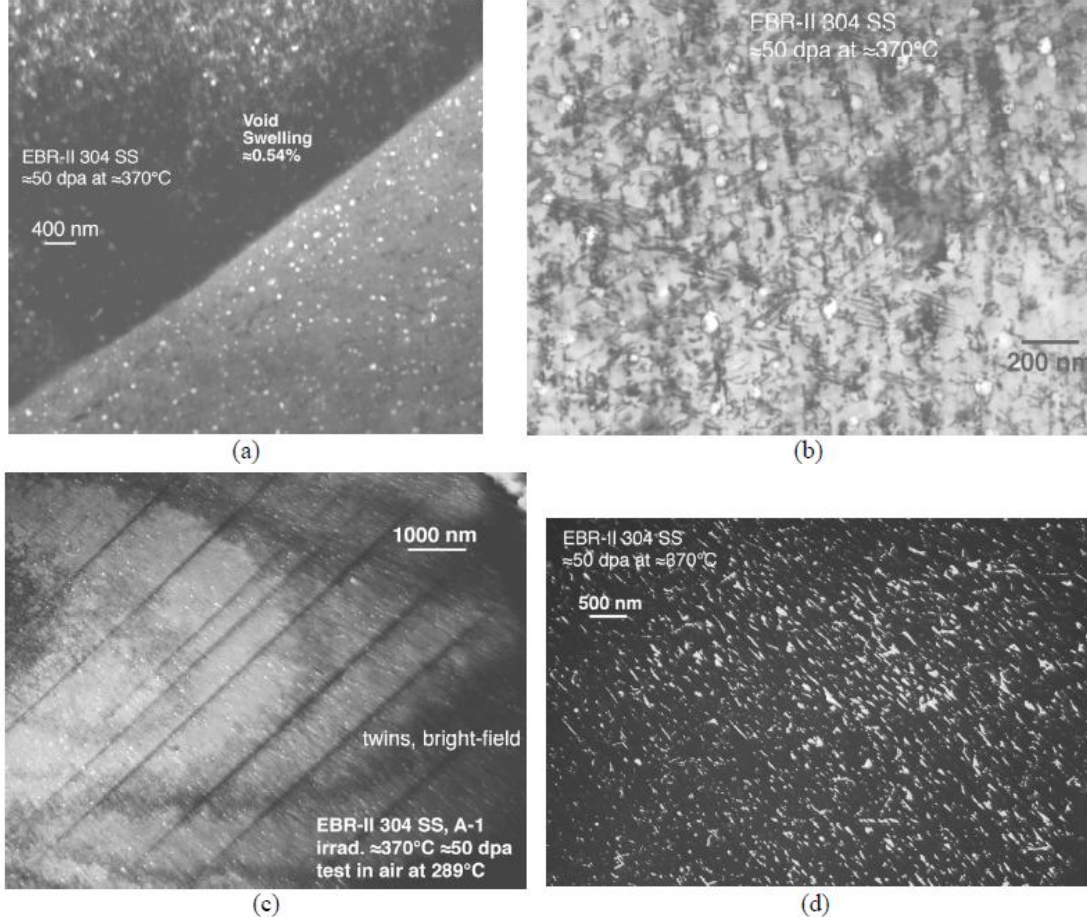


Figure 5. Microstructure of SA Type 304 SS fuel subassembly hex can irradiated in EBR-II at 370 °C to 50 dpa; (a) voids near grain boundary, (b) high magnification, (c) voids and twins in low magnification, and (d) dark-field image of dense carbide precipitates. (From [10])

Helium also plays a significant role in void swelling. As a natural product of the fission process (in the form of alpha radiation), helium is known to have a significant effect in accelerating void formation. A study by Lee et al examined the void formation and changes in microstructure and mechanical behavior of austenitic steel when irradiated with He ions as opposed to other forms of ion radiation [11]. The results show that the voids formed in the material were larger than those formed from other

irradiation types (at relative doses and dose rates). Olander also postulates that the incubation period ( $\sim 10^{22}$  n/cm $^2$ ) may be directly related to the time needed for transmutation of helium produced by irradiation to start the formation of voids [2].

#### ***d. Embrittlement and Loss of Fracture Toughness***

Another detrimental phenomenon brought about by irradiation is the effect on fatigue and toughness in FCC and BCC metals. Ferritic/martensitic steels such as HT9 will experience a reduction in fracture toughness which is noted by a higher ductile-to-brittle transition temperature (DBTT) and lower upper shelf energy (USE) obtained via a Charpy impact test (austenitic steels, however, do not experience DBTT) as seen in Figure 6. The magnitude in DBTT change is inversely proportional to the irradiation temperature [12].

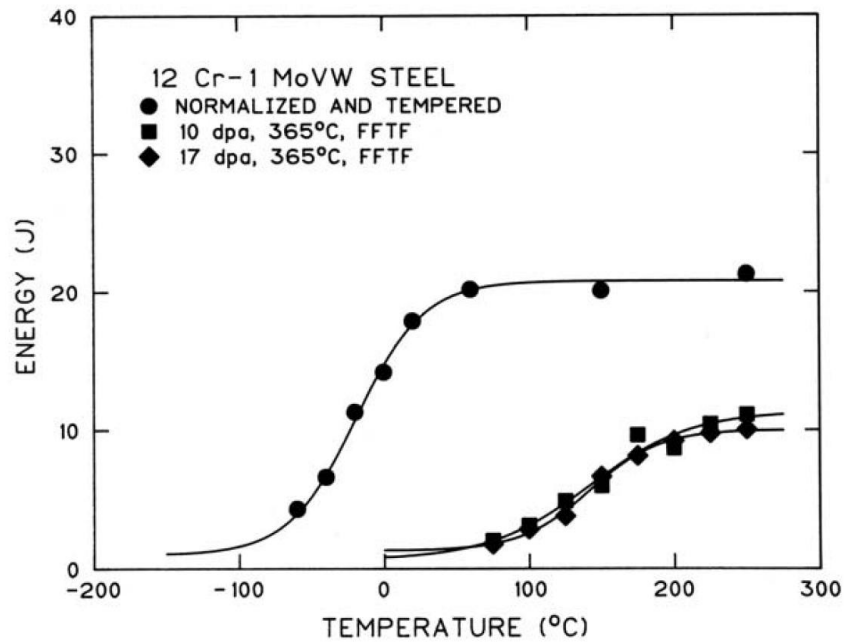


Figure 6. Charpy impact curves for Sandvik HT9 (12Cr-1MoVW) in the unirradiated condition and after irradiation to 10 and 17 dpa at 365 °C in Fast Flux Test Facility (From [12]).

An example of one such phenomenon that leads to a higher DBTT is the observed diffusion of phosphorus to grain boundaries. In the presence of neutron irradiation, Little postulates two mechanisms based upon phosphorus segregation [3]:

- (1) Irradiation assisted phosphorus segregation where phosphorus, as an undersized solute, couples with self-interstitial point defect flux and migrates to interfaces.
- (2) Segregation via normal vacancy controlled mechanism, but augmented by the irradiation-induced vacancy flux over longer time periods.

*e. Irradiation Creep*

In general, creep refers to the slow, time-dependent deformation of a material while subjected to a tensile stress. Irradiation creep can be separated into two general categories: irradiation-enhanced creep (which is the enhancement of thermal creep by irradiation), or irradiation-induced creep (deformation of an irradiated material in the absence of thermal creep).

Two mechanisms enhance irradiation-induced (low temperature) creep. The first is the climb of dislocations in the material by way of migration of vacancies toward the dislocation (transient creep). The second is mechanism is the deformation by way of collapsing dislocation loops [2]. The combinations of these two mechanisms enhance the ability of dislocations to climb over obstacles until glide is again possible. As the dislocations climb over obstacles, there is a subsequent stress release, which referred to as stress relaxation. From a technical standpoint, this relaxation of residual stresses may be beneficial. However, Was postulates that the elevated creep rates (in excess of thermal creep) may raise the susceptibility, initiate, and sustain stress corrosion cracking. Creep also relieves compressive stresses (such as surface peening), which degrade the intended effects of fatigue and crack minimization [1].

**2. Design Considerations for Materials in Nuclear Applications**

While considerable research has been devoted to the use of fusion as the future of nuclear power, commercial nuclear power plants currently in operation employ fission as their heat source. Fission plant characteristics vary in fuel selection, coolant type, neutron fission energy, and normal operating temperature and pressure to name a few. Plant examples are listed in Table 1.

Table 1. Typical thermodynamic and fuel characteristics for six reference power reactor types: boiling water reactor(BWR), pressured water reactor(PWR), pressurized heavy water reactor (PHWR), high-temperature gas reactor(HTGR), advanced gas-cooled reactor(AGR), and liquid metal fast breeder reactor(LMFBR) (From [13]).

Characteristic	BWR	PWR	PHWR	HTGR	AGR	LMFBR
<b>System</b>	BWR/6	Sequoyah	CANDU-600	Fulton	HEYSHAM 2	Superphenix
<b>Neutron Energy</b>	Thermal	Thermal	Thermal	Thermal	Thermal	Fast
<b>Fuel</b>	$^{235}\text{U}$	$^{235}\text{U}$	$^{235}\text{U}$	$^{235}\text{U}$	$^{235}\text{U}$	$^{239}\text{Pu}$
<b>Cladding Material</b>	Ziracaloy-2	Zircaloy-4	Zircaloy-4	Graphite	Stainless Steel	Stainless Steel
<b>Primary coolant</b>	$\text{H}_2\text{O}$	$\text{H}_2\text{O}$	$\text{D}_2\text{O}$	He	$\text{CO}_2$	Liq. Na
<b>Pressure(MPa)</b>	7.17	15.5	10.0	4.90	4.30	~0.1
<b>Ave. outlet temp(<math>^{\circ}\text{C}</math>)</b>	288	324	310	741	635	545

In addition to the same design considerations extended to conventional power plants (nominal thermal and hydraulic conditions, corrosion resistance, mechanical behavior, etc.), materials in nuclear applications must also be engineered to withstand the harsh environment as a result of neutron irradiation. Structural components must be made of material that can resist damage due to years of irradiation and experience the minimal amount of neutron activation. Developing a new alloy or improving upon alloys currently in service is the main motivation behind this work.

### 3. Alloy 316 Stainless Steel and its Application in Nuclear Engineering

Alloy 316 steel is an iron-based, austenitic (FCC) crystal structure with nickel and chromium as their major alloying constituents; hence it is commonly referred to as chrome-nickel steel. The addition of nickel stabilizes the austenite phase with the FCC

structure, which promotes higher ductility and toughness, especially at lower temperatures. The remaining constituents of austenitic stainless steels are either interstitial or substitutional impurities, and are listed in Table 2:

Table 2. Nominal composition of Alloy 316 including the function of each alloying element  
(From [14]).

Element	wt %	Function of Alloying Element
Fe	64	-
Cr	~17	General corrosion resistance
Ni	~12	Promotes austenitic crystal structure
C	0.08	Increases mechanical strength, promotes austenitic structure
Mn	2	Improves hot ductility
Si	1	Increases resistance to oxidation
P	0.045	(trace impurity)
S	0.03	(trace impurity)
Mo	~2.5	Increases resistance to general and localised corrosion

Austenitic stainless steels have several advantages in general use. Their primary desirable characteristic is that stainless steels are resistant to general corrosion. They have moderate yield strength (~205MPa) which can be cold-worked to further improve it. Stainless steels are relatively resistant to high-temperature creep up to approximately 538°C [15].

In nuclear power generation applications, austenitic steels have historically been used for reactor core materials. Reactor cladding is the crucial metallic component in the core. The cladding provides structural integrity for the fuel. It serves as a boundary to prevent both fission products from escaping to the core coolant, and segregates the fuel from the coolant to prevent erosion and reaction between the two [2]. For liquid metal fast breeder reactors (LMFBR), Type 316 steel was originally used as cladding for the uranium oxide ( $UO_2$ ) fuel in the core. It resists corrosion by the fuel matrix on the inner surface of the cladding and the liquid sodium coolant on the outer surface. Additionally, stainless steel can be used as cladding material because austenitic steel does not affect neutron economy for neutrons at fast fission energies. Because stainless steel has a

tendency to absorb and interact with neutrons at thermal energies, stainless steel is used primarily for structural support in pressurized water (light water) reactors, or PWRs, as seen in Figure 7.

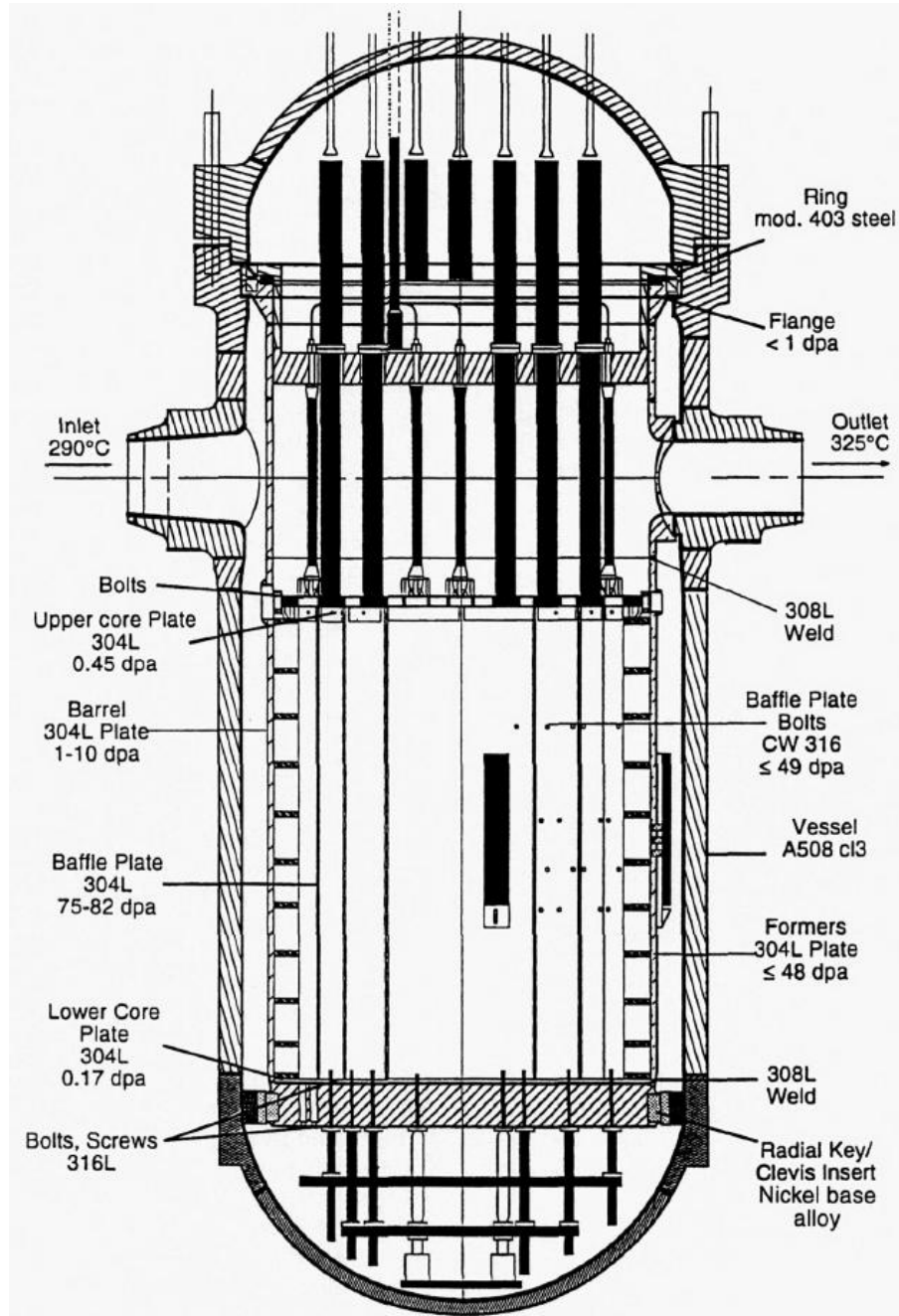


Figure 7. Schematic diagram of core internals of a PWR indicating typical material and end-of-life displacement dose ranges (From [3]).

There are, however, certain problems associated with the use of austenitic stainless steel in nuclear reactors components. Stainless steels are susceptible to the following phenomena[1], [2].

1. Void formation due to irradiation, which ultimately leads to swelling of the material (and thus limits the operating lifetime of the material)
2. High-temperature embrittlement by helium (which is produced as a result of the fission process).
3. Irradiation-assisted stress corrosion cracking (IASCC), which is a form of inter-granular stress corrosion cracking brought about by RIS.

The transition from thermal fission reactor design to fast fission LMFBRs presented challenges due to the typical operating conditions in a fast fission reactor. By comparison, fast fission neutron energies are greater than 0.2 MeV, and the neutron flux is on the order of 100 times greater than that of thermal (< 0.2 MeV neutron energy) reactors [2]. The original cladding material choice for prototype LMFBRs during development was austenitic steel. The Prototype Fast Reactor (PFR), developed in the UK, was built with austenitic steel structural materials. The PFR design utilized a free-standing reactor core design where the fuel assemblies were cantilevered to bottom core supports. Post-testing inspection of the PFR fuel assemblies revealed significant axial and radial distortion in the fuel assemblies due to void swelling, in addition to bowing and buckling of the fuel assembly wrappers, as seen in Figure 8.

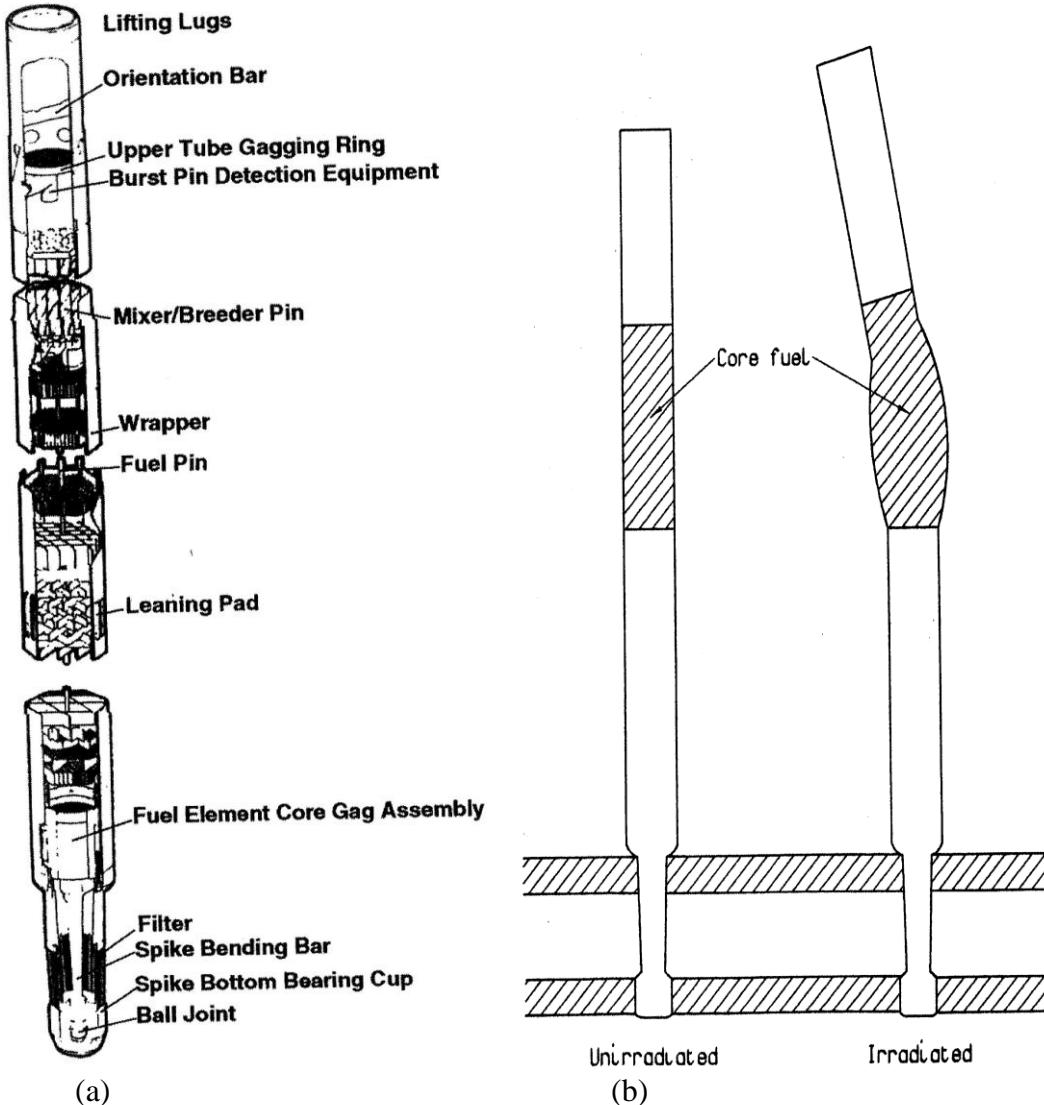


Figure 8. a) PFR standard core subassembly. b) Fast reactor core fuel element subassembly bowing, dilation, and length increase resulting from irradiation (From[16])

Previous studies had already established that void formation and swelling, helium embrittlement, and RIS become more pronounced as a direct function of time and neutron flux. Given the test results from PFR and other prototype fast fission reactors, it became imperative to find a suitable material capable of withstanding the higher neutron flux and operating temperatures.

The demand for continued production of commercial energy (and the desire to maximize the serviceable lifetimes of reactor plants) has put the study of these detrimental effects to the forefront in the field behavior of nuclear materials. This is one of the major motivating elements for this thesis research.

#### **4. Alloy HT9 Ferritic/Martensitic Steel and its Application in Nuclear Engineering**

Like other classes of ferritic/martensitic steels (also referred to as high-chromium steels), Alloy HT9 is characterized by a predominantly body-centered cubic (BCC) crystal structure (the martensite component is body-centered tetragonal, or BCT) with chromium as its major alloying element. In comparison to austenitic and other carbon steels, ferritic/martensitic steels can be significantly stronger and harder with the proper heat treatment (alloy 9Cr-1MoVNb steel, for instance, has a yield strength of approximately 450 MPa compared to 290 MPa for alloy 316SS) [12].

Alloy HT9 is the first of three generations of ferritic/martensitic steels specifically designed for elevated-temperature application dating back to the 1970s; HT9 was designed for a maximum operating temperature of 565 °C (1049 °F) [7], [12]. The nominal composition of HT9 is shown in Table 3:

Table 3. Nominal composition of Alloy HT9 including the function of each alloying element (From[12], [14])

<b>Element</b>	<b>wt %</b>	<b>Function of Alloying Element</b>
Fe	84.55	-
Cr	12	Limited corrosion resistance, promotes ferritic crystal structure
Ni	0.5	Increases toughness
C	0.2	Increases mechanical strength
Mn	0.6	Promotes austenite to ensure full martensite transformation
Si	0.4	Increases resistance to oxidation, promotes ferritic structure
W	0.5	Ferrite stabilizer, substituted for Mo for nuclear (reduced-activation) application, carbide former
S	0.03	(trace impurity)
Mo	1.0	Increases resistance to general and localised corrosion
V	0.25	Strong carbide former

The original motivation for the development of high-chromium steels was for use in fossil-fuel conventional power plants, with the most notable benefit being their resistance to high-temperature creep relative to other steel grades. With increasing demand for nuclear power, ferritic/martensitic steels have replaced austenitic steel as the cladding material of choice in fast fission reactor plants and have been eyed as a candidate for fusion reactor first-wall material due to its more desirable material characteristics. High-chromium steel exhibits better thermal conductivity, lower thermal expansion, and significantly higher resistance to void swelling than austenitic stainless steels as seen in Figure 9 [12]. Little suggests that this resistance to swelling is due (in part) to the strain fields generated in BCC iron from small interstitial solutes such as carbon and nitrogen. These strain fields interact with the radiation-induced point defects and dislocations to promote recombination of the point defects, ultimately minimizing void nucleation and growth [3].

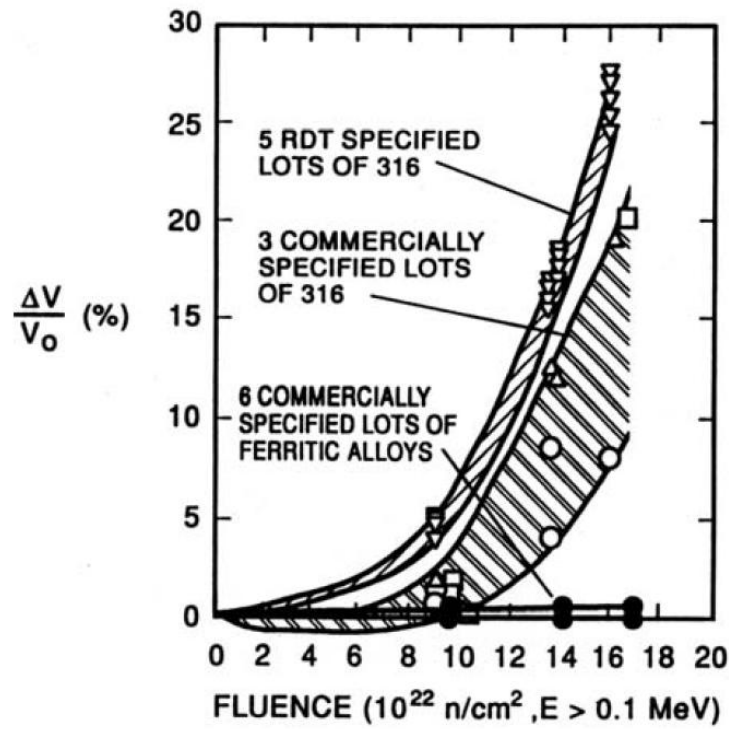


Figure 9. Swelling behavior of six commercial heats of ferritic/martensitic steels compared to type 316 stainless steel after irradiation in Experimental Breeder Reactor-II at 420 °C to ~80dpa (From [7]).

Additionally, high-chromium alloys are less susceptible to inter-granular cracking and IASCC than its predecessors. The multiple benefits over austenitic steel make them ideal for fuel cladding, wrappers, and ducts in fast-fission reactor plants [12].

The international community in recent years has collaborated to develop a new generation of reactor plants (known as Generation IV) in which the predicted normal operating temperatures and pressures exceed those of current-day fission reactors. Because of this, an emphasis has been placed on developing future ferritic/martensitic steel that can withstand operating temperatures in excess of 650°C. Current generation ferritic/martensitic steels (Generation 3) have a maximum operating temperature of 620 °C; and thus, a new family of HT9-like alloys must be developed for next-generation reactor core materials in the United States.

Additionally, alloy HT9 (among other ferritic/martensitic variants) has been considered a candidate for first wall and fusion shield/blanket material in fusion reactors such as the tokomak fusion reactor shown in Figure 20. In the fusion reaction, fast neutron energies are 7 times that of a fast neutron born from fission. It is currently difficult to study the effects of neutron flux and the radiation damage associated with fusion, since test facilities lack the ability to generate neutrons with fusion energies. The closest simulations to fusion energy are by using ion accelerators, and the test samples are constrained to small specimens [16]. Therefore, further studies are needed to better simulate and understand the effects on candidates for first wall and fusion blanket material.

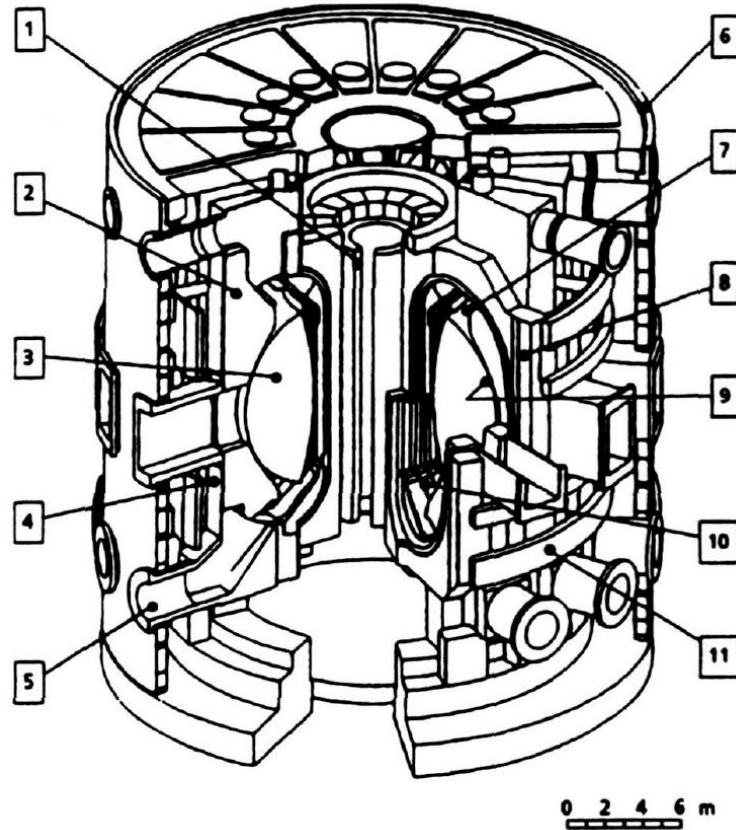


Figure 10. Key components of the tokomak fusion reactor: 1 – central solenoid; 2 – shield/blanket; 3 – plasma; 4 – vacuum vessel shield; 5 – plasma exhaust; 6 – cryostat; 7 – active coil; 8 – toroidal field coils; 9 – first wall; 10 – divertor plates; 11 – poloidal field coils (From [3]).

### C. SOLID SOLUTION MODIFICATION FOR IMPROVED REACTOR STEEL PERFORMANCE

New alloys based upon solid solution additions to existing reactor steels may provide a route to enhanced steel performance while maintaining cost requirements applications of new materials. The objective in developing an alloy for an engineering application is to achieve and maximize quality, performance, and safety margin while minimizing cost and adverse effects associated with the combination of the chosen alloying agents. Alloying, in the simplest of terms, is the mixing of an alloying agent (typically referred to as a solute) into a base material (solvent) to form a solid solution. The following are notable benefits that can be achieved by alloying relevant to this research.

Solid solutions of iron with other metallic solutes can increase the high temperature yield strength of reactor steels. The lattice structure of pure metals at equilibrium allows significant mobility of dislocations when a shear stress is applied. By adding a substitutional solute with a dissimilar atomic radius than the base metal's atomic radius (whether larger or smaller), the solute atoms impose lattice strains on the surrounding atoms. Substitutional atoms with larger atomic radii generate compressive lattice strains while atoms with smaller atomic radii impose tensile strains. Atoms with extremely small atomic radii relative to the lattice go on to form interstitial solid solutions. Some common alloying elements are shown in Table 4.

Table 4. Atomic radii and percent mismatch of each refractory element in relation to the atomic radius of iron. Included in this table are values of other alloying candidates for addition to steel to mitigate adverse effects of neutron irradiation. (Atomic radii values From [17])

Element	Atomic radius [nm]	Solute mismatch to iron
Fe	0.124	-
Cr	0.128	3.23%
Mo	0.136	9.68%
Nb	0.143	15.32%
Ta	0.146	17.74%
W	0.137	10.48%
Pt	0.139	12.10%
Zr	0.159	28.23%
Hf	0.155	25.00%

With these lattice strains present, more force is required to move dislocations through a lattice with solutes relative to a lattice of pure metal [18]. This phenomenon is known as solid solution strengthening. The resultant solid solution becomes harder and has a higher yield and tensile strength at the expense of being more brittle, less ductile, and less tough. Because this thesis will examine the effects of various solid solutions, it is notable to mention that interstitial solid solutions have significantly larger strengthening effects than those of substitutional solid solutions. An example of this application in steels is the interstitial strengthening effect of carbon (atomic radius of 7.1pm) relative to that of substitutional manganese (atomic radius of 112pm) [17].

## **1. Addition of Oversized Solutes to Mitigate RIS in Austenitic Stainless Steel**

Radiation-induced segregation is postulated to exacerbate IASCC, and thus poses a serious safety concern in contributing to failure in reactor components built of austenitic steel. The addition of oversized solutes to austenitic steel has been examined in an attempt to mitigate the effect of RIS, thus reducing susceptibility to IASCC.

Early work by Sakaguchi and Shigenaka examined the effects of addition of Ti, Nb, Zr, Hf, Mo, and Si to austenitic steel prior to irradiation. Shigenaka concluded that the addition of Mo suppresses heterogeneous loop nucleation and Si acts as a nucleus to form Mo-Si clusters in stainless steel. Sakaguchi concluded that the effect of Hf and Zr on mitigating RIS-induced grain boundary segregation was more significant than that of Ti or Nb due to the significantly larger size of the Hf and Zr atoms [19].

Later work by Hackett, Busby et al. studied in more detail the effects of adding Hf and Zr to Alloy 316 steel in mitigating RIS. Hackett theorizes that oversized solutes enhance the recombination of radiation-induced defects via a solute-vacancy trapping process. By limiting the diffusion of defects to the grain boundaries, one in turn limits the diffusion of Cr away from them. In their work, solutes produced limited results in that RIS was reduced, but the effects of Zr and Hf all but disappeared for neutron damage in excess of 3–7 dpa, depending on the irradiation temperature [19].

Gan, Simonen et al. also investigated the effects of solute additions of Hf and Pt in Alloy 316SS. They concluded that Hf strongly suppressed microstructure evolution in Ni-ion-irradiated steel up to 50 dpa by forming fine Hf precipitates. The alloying of platinum, which consequently failed to form precipitates in the steel, showed no beneficial effect in mitigating microstructural change [5].

## **2. Evolution of Ferritic/Martensitic Steel for Reduced Activation and Higher Creep-Rupture Strength in Nuclear Applications**

As mentioned previously in section I.B.4, high-chromium, ferritic/martensitic steels were initially developed with fossil-fuel power plant operation in mind. Subsequent generations of these steels were geared toward reactor plant operation where

these materials would be subjected to large neutron fluence over the lifetime of the plant. Alloying elements such as Mo, Nb, and Ni become highly radioactive when irradiated, thus posing an operational hazard and a radiation waste hazard. More recent ferritic/martensitic alloys have sought to lower neutron activation of the steels by replacing Mo, Nb, and Ni with W, V, and Ta. Tungsten and vanadium are utilized for their carbide-forming ability; tantalum, however is utilized as an austenite grain refiner for the heat treatment process. Ta and W have also been studied as substitutes for other carbide formers because of their resistance to neutron activation [3].

In anticipation of subjecting high-chromium steels to higher maximum operating temperatures, the need for higher creep-rupture strength is warranted. To achieve higher resistance to high-temperature and irradiation-induced creep, the alloying of the various carbide formers (as described in Table 3) have been studied. As an example, third-generation ferritic/martensitic steels (e.g., EUROFER, F82H, modified 9Cr-1Mo, and NF616) have seen the substitution of W for some (or all) of Mo and have included boron to achieve higher rupture strengths, as seen in Figure 11.

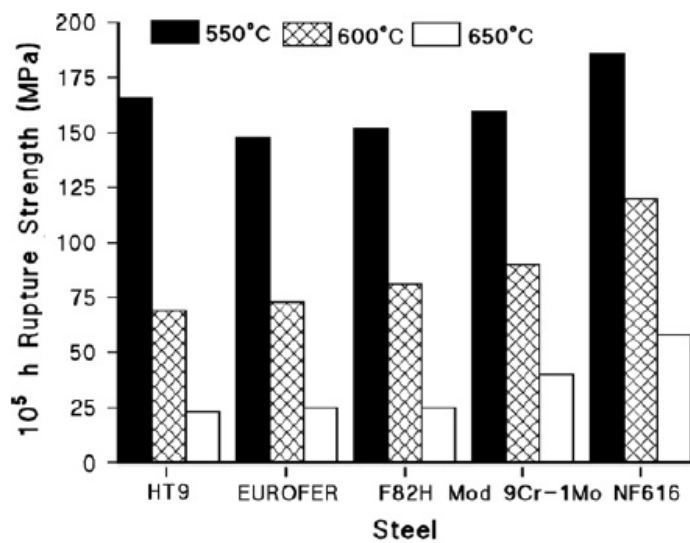


Figure 11. A comparison of 100000 h rupture strengths for Sandvik HT9, EUROFER, F82H, modified 9Cr-1Mo, and NF616 at 550, 600, and 650 °C (From [12]).

#### **D. DIFFUSION COUPLE AND MULTIPLE APPROACHES: A HIGH THROUGHPUT METHOD FOR RAPID ALLOY DEVELOPMENT**

Timely development of new alloys requires new experimental approaches that reduce the time and cost required to screen new alloy compositions. For example, examining four new alloy additions (e.g., Ta, W, Nb, and Mo) at four compositional levels (e.g., 1, 2, 3, and 4 weight percent) would require the development of 256 individual alloy heats to examine all unique combinations. Clearly this number of individual experiments can quickly become cost prohibitive and can extend beyond the boundaries of a reasonable alloy development program.

High-throughput experimentation, or HTE, is a relatively new combinatorial research discipline that fuses analytical methods with recent advances in materials research. HTE couples measurement tools capable of performing parallel experimentation of samples with informatics to compile a library of result data. This discipline has become a staple in the chemical, pharmaceutical, and polymer industry because of the wealth of data mined at a fraction of the cost [20].

One combinatorial approach for screening new alloys is the use of diffusion couples or multiples. In the diffusion couple or multiple approach, two or more metals are placed in intimate contact, subjected to high temperature and pressure, and then annealed for a period of time to allow significant inter-diffusion between the alloying additions of interest [21]. The process results in the creation of an equilibrium composition gradient of one species into another, separated by an intermetallic region at the diffusion couple interface.

A library of information can be gathered from a single diffusion couple. This method can be utilized as a time- and cost-saving technique in conjunction with traditional metallurgical methods of batch alloying. The myriad of compositional combinations can enable an alloy developer to preemptively weed out non-useful alloy combinations and focus on those that show promise in their engineering properties.

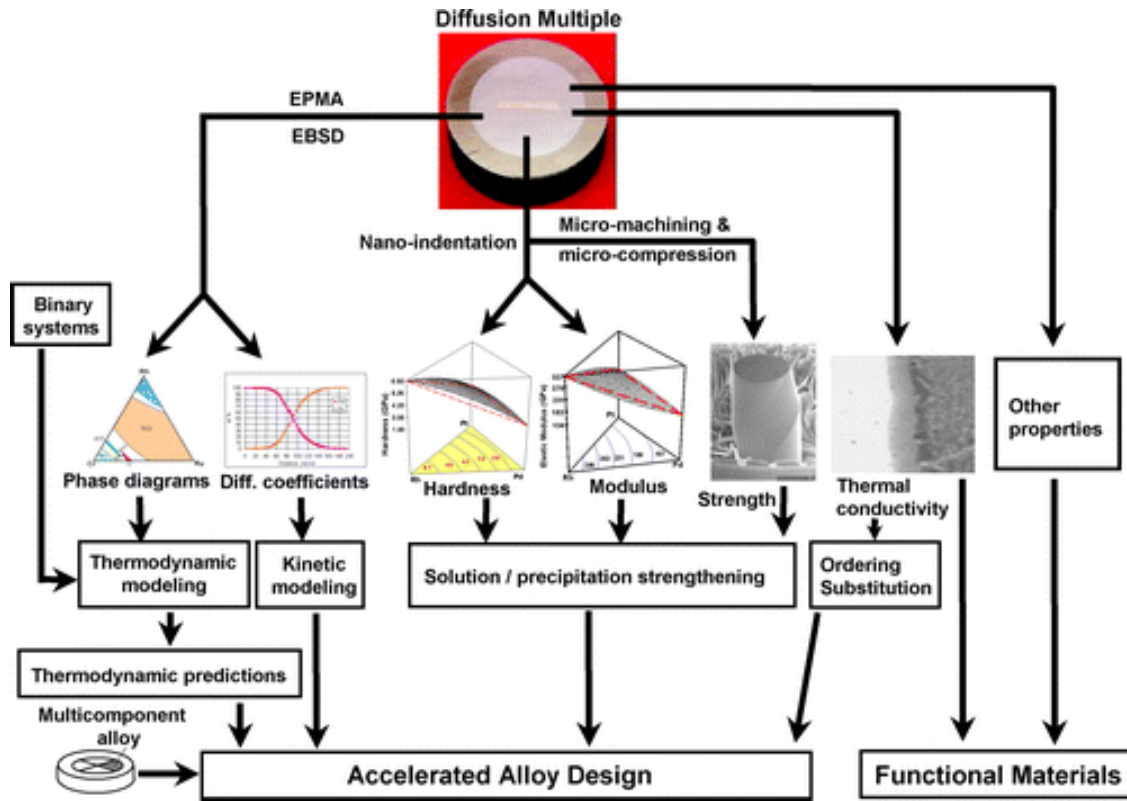


Figure 12. Flow diagram of informatic processes utilized in the diffusion multiple approach (From [21]).

Mechanical properties such as hardness and Young's modulus can be determined via nanoindentation, while material characterization and crystal structure can be analyzed via energy dispersive x-ray spectroscopy (EDS) and electron backscatter diffraction (EBSD), respectively. From a single diffusion couple one can determine equilibrium data for mapping phase diagrams. Additionally, one approximate the solubility limit of an alloying element, i.e., to what amount the element can be added before undesirable topologically close-packed (TCP) intermetallics and two-phase regions form [20].

## E. THESIS QUESTIONS

This thesis will utilize the diffusion couple approach to analyze the potential benefits and limitations of Mo, Nb, Ta, and W in 316SS and HT9 ferritic/martensitic steels. The diffusion couple samples were prepared by Sandia National Laboratories and sent to Naval Postgraduate School (NPS) for analysis. The diffusion couples in this work were as follows:

Table 5. Diffusion Couples Available for Analysis

Refractory Element	316SS	Alloy HT9
<b>Mo</b>	X	X
<b>Nb</b>	X	
<b>Ta</b>	X	X
<b>W</b>	X	X

This thesis was organized around the following questions:

**1. What is the Maximum Amount of Refractory Element that can be Added in Each Alloy before the Solubility Limit is Reached?**

The solubility limit is defined as the “maximum concentration of solute atoms that may dissolve in the solvent to form a solid solution” [18]. When the diffusion couples are fabricated, the annealing process promotes diffusion of the refractory element into the steel. The refractory element concentration in the base metal (either 316SS or HT9) will increase with closer proximity to the interface until this solubility limit is reached. Once this solubility threshold is passed, the refractory element composition remains relatively constant up to the formation of intermetallic compounds. Formation of distinct phases other than a homogeneous solid solution past the solubility limit will be present in the form of laves (intermetallic) phases or that of a two-phase region, as seen in Figure 13. This work will attempt to catalog and compare the relative solubility limits for the refractory elements in alloy 316SS and alloy HT9.

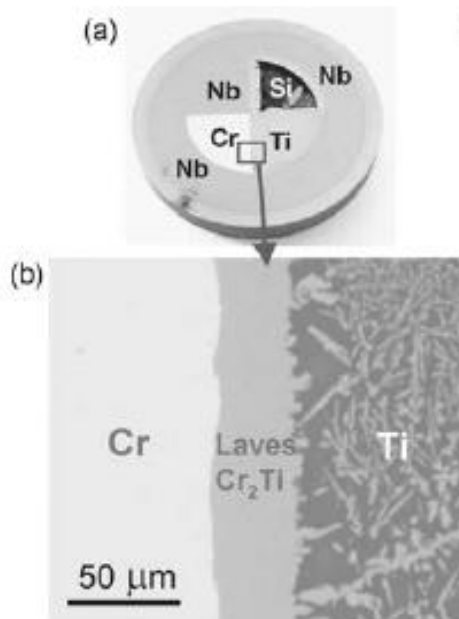


Figure 13. (a) optical image of a Nb-Ti-Si-Cr diffusion multiple; (b) EPMA Cr map of the Cr-Ti binary diffusion couple region showing the formation of Laves phases ( $\text{Cr}_2\text{Ti}$ ) and precipitation of the C-15 Laves phases from bcc(Ti,Cr) during sample cooling from 1100°C to room temperature (From [21]).

## 2. What is the Relative Diffusivity for Each Refractory Element in Alloy 316 and Alloy HT9?

This work will apply a fundamental 1-D diffusion analysis to examine the kinetic aspects of the refractory element diffusion in each alloy. Understanding the magnitude of the diffusivity will form the basis for understanding the radiation-induced enhancement in refractory element diffusivity in alloys 316SS and HT9.

## 3. What is the Change in Hardness, Yield Stress, and Young's Modulus with the Addition of the Refractory Element?

Yield stress and hardness are directly proportional to one another; that is, if one can identify an increase in hardness in a material, then it can be assumed that its yield strength is also higher. This work will attempt to correlate solute concentration (via quantitative energy dispersive spectroscopy, or EDS) and hardness (via nanoindentation)

to determine if the addition of the refractory element contributes to a proportional change in yield strength. A similar comparison will be made between solute composition and Young's modulus.

#### **4. Is the Diffusion Couple Approach a Useful Tool in Reactor Steel Development?**

Experimental results will attempt to determine if this high throughput method can be used to successfully model and/or evaluate refractory additions in reactors steels. This work will examine potential shortfalls with the diffusion couple approach in alloy development. One such example would be the excessive thermal expansion mismatch between the refractory element and the base metal during fabrication, which could inhibit diffusion due to lack of contact between refractory element and the base metal.

Additionally, the formation of the intermediate intermetallic phases from diffusion couple fabrication may provide useful information about the mechanical behavior of materials subject to irradiation-induced grain boundary segregation.

## II. METHODS

### A. DIFFUSION COUPLE FABRICATION

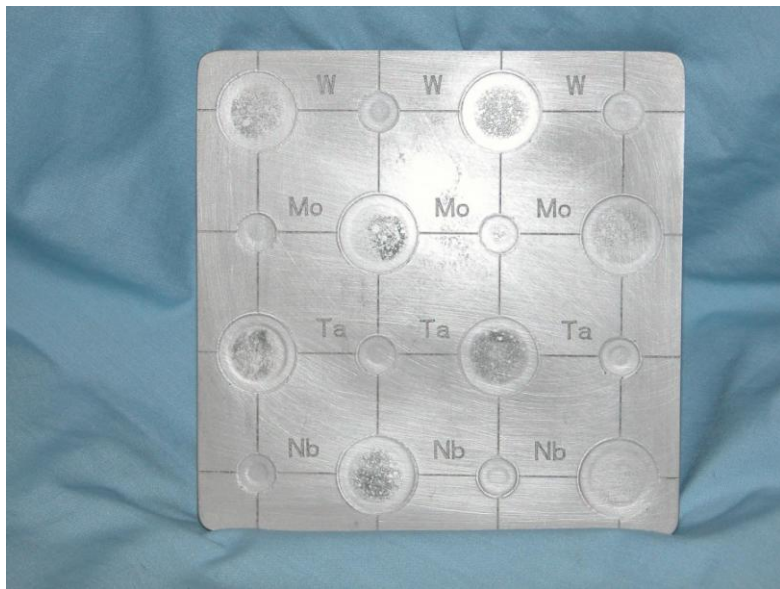
Diffusion couples were made for both 316 stainless steel and HT9 ferritic martensitic steel at Sandia National Laboratories. The 316 stainless steel had a certified composition of:

Fe-16.34Cr-10.03Ni-2.03Mo-1.321Mn-0.610Si-0.025N 0.024P-0.019C-0.008S

The HT9 steel was provided by Los Alamos National Laboratory and had a nominal composition of Fe-12Cr-1MoVW-0.18C.

Refractory metal sheets 1mm in thickness were purchased from Eagle Alloys at a purity of 99.9%.

For both diffusion couples, the design consisted of a single block of 316 steel into which 10 mm deep, cylindrical holes were milled (Figure 14). These holes had diameters of 6 mm and 18 mm. Disks of either 316 steel or HT9 steel with a central, 1mm thick disk of a given refractory metal were placed into these holes. The refractory metals disks were metallographically polished on both sides. Each diffusion couple block contained 16 separate diffusion couples, four for each refractory metal with two of each diameter.



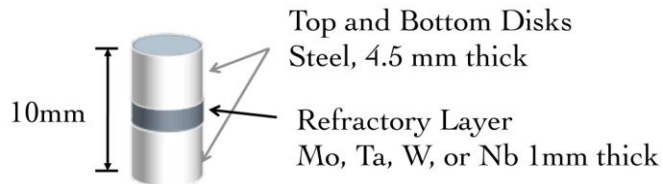


Figure 14. (Top) Photograph of diffusion couple block after hot isostatic pressing. (Bottom) Schematic of diffusion couple cylinders.

After assembly, the diffusion couple blocks were welded closed in a vacuum of  $10^{-5}$  torr. The diffusion couple blocks were then hot isostatically pressed at 1100°C for 2 hours at a pressure of 100 MPa under argon. After hot isostatic pressing, the diffusion couple blocks were heat treated in a vacuum furnace at 1100°C for 400 hours. The HT9 block was given one additional heat treatment to try to restore the martensitic microstructure.

Diffusion couple samples were prepared using metallographic techniques. Rectangular samples were sectioned from the diffusion-bonded cylinders using electro-discharge machining (EDM). The sectioned samples were then polished on one side using metallographic techniques down to a diamond finish of 1 micron. The final surface polishing involved vibratory polishing overnight with a colloidal silica suspension (50nm average particle size). An example of the finished specimen can be seen in Figure 15.

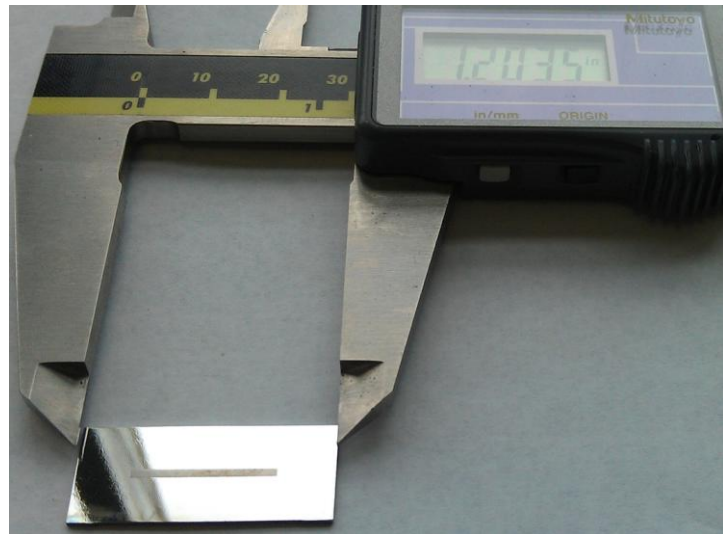


Figure 15. Diffusion couple coupon after sectioning and polishing as received from Sandia National Laboratories.

## **B. MATERIAL CHARACTERIZATION**

### **1. Equipment**

All optical imaging was performed on a Nikon Epiphot 200 optical microscope with digital images generated using NIS Elements software. Electron microscope imaging and x-ray energy dispersive spectroscopy (EDS) analysis were performed using the Zeiss Neon 40 Field Emission Scanning Electron Microscope (SEM) with Focused Ion Beam (FIB) and the Apollo EDS Silicon Drift Detector (SDD) at Naval Postgraduate School, Monterey. Quantitative characterization (EDS) was performed using EDAX Genesis software.

### **2. Assumptions**

The focus of the material characterization phase was to assess the phase and microstructural changes caused by interdiffusion of refractory elements into steel and to quantitatively determine the compositional variations (in the form of EDS spectra) in relatively close proximity (<1mm from) to the diffusion couple interface in order to correlate microstructure and composition to mechanical property data obtained through nanoindentation.

Because the compositional data were to be obtained close to the interface, this study operated under the assumption that diffusion occurred in a one-dimensional direction perpendicular from the refractory element bar, being assumed uniform as a function of depth below the surface as well as parallel to the interface. Therefore, the amount of inter-diffusion (and composition) of alloy species would be the same for a given distance from the interface as illustrated in Figure 16.

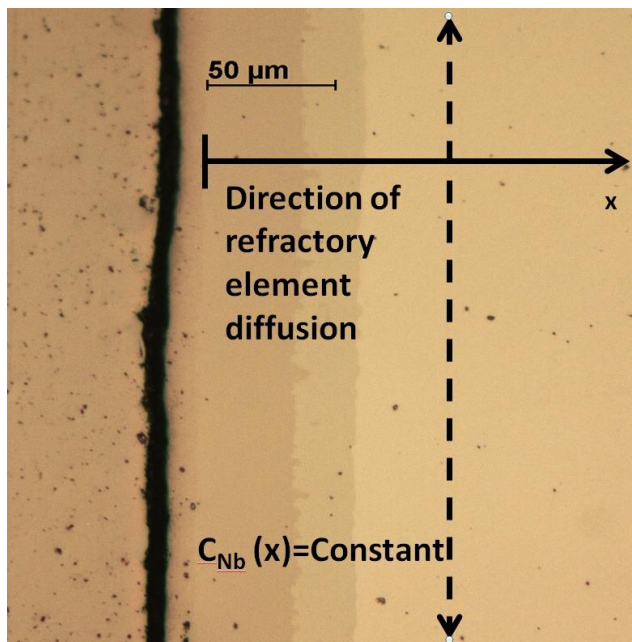


Figure 16. Visual representation of the assumption of 1-D diffusion on solute refractory element composition, Nb/316SS diffusion couple, optical image.

The assumption of constant composition, however, loses its validity in certain cases where large amounts of interdiffusion occurred, resulting in multiphase regions close to the interface as seen in Figure 17. Thus, the sample points were chosen such that these regions were avoided.

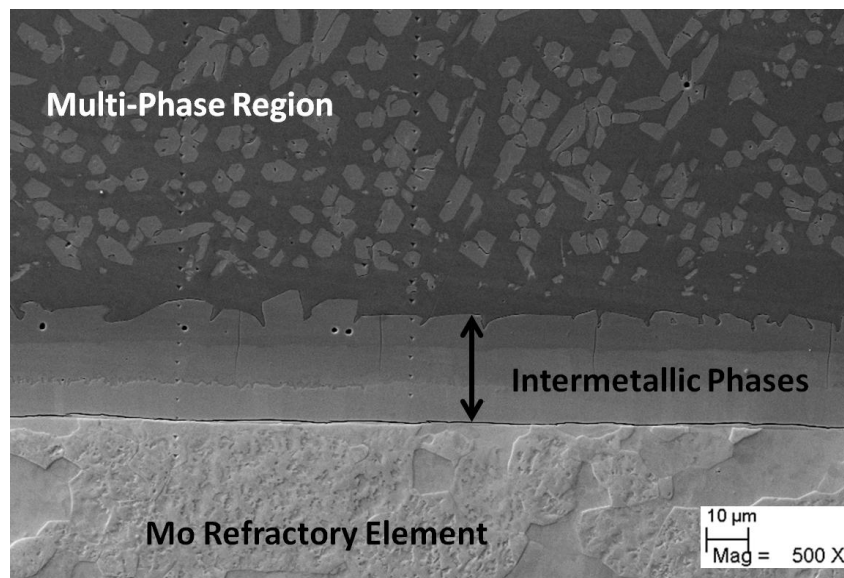


Figure 17. SEM Image of Mo/HT9 diffusion couple interface showing the intermetallic and multi-phase regions.

### 3. Experimental Procedure and Parameters

Quantitative x-ray analysis was performed by use of pure element and compound standards. Part of this evolution involved the generation of a pure element standards library since one had not been previously recorded for the Zeiss SEM on campus. The quantitative analysis procedure defined by Goldstein et al. was performed as follows [22].

#### *a. Obtaining X-ray Spectrum of the Standards and Specimen under Defined and Reproducible Conditions*

Care was taken to ensure that the SEM parameters during pure standards EDS were the same as those used in collection of x-ray spectrum from the diffusion couples. The defined parameters and their values are as follows:

Table 6. SEM Parameters used in pure standards and experimental EDS.

Parameter	Value
<b>Objective Aperture</b>	60 $\mu\text{m}$
<b>Working distance</b>	5 mm
<b>Dead time percentage</b>	25–45%
<b>Sample time</b>	100 sec (live time) per point
<b>Amplifier time constant</b>	12.8 $\mu\text{s}$
<b>Beam voltage</b>	20 kV
<b>Beam current</b>	$1.32 \times 10^{-6}$ mA
<b>Take-off Angle</b>	30.0 degrees

The UHV-EL-37H standard block by Geller MicroAnalytical Laboratories (illustrated was used for this experiment).

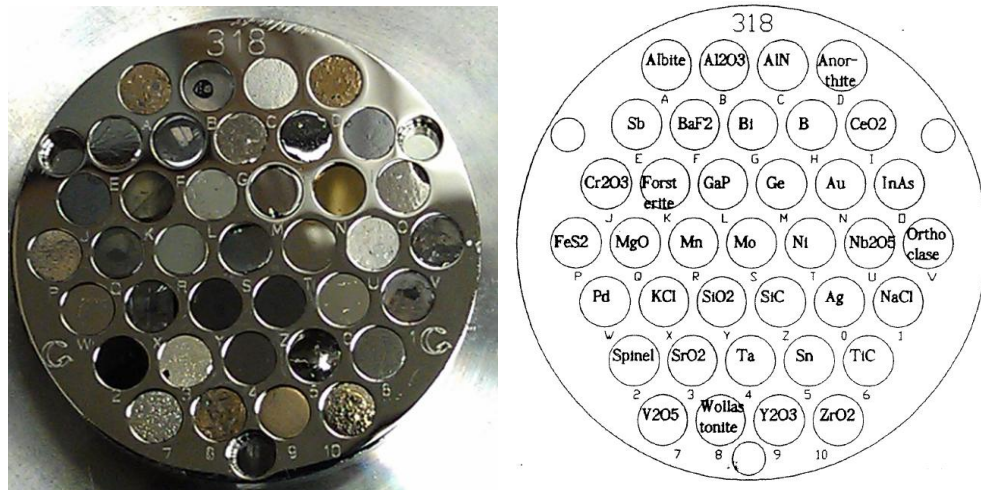


Figure 18. Geller pure standards block with associated element/compound map.

**b. Measuring Standards Containing the Elements that have been Identified in the Specimen**

Based on the major alloying elements in 316SS and alloy HT9, the following element compositions were measured under the above, prescribed conditions:

Table 7. Pure standards used for quantitative analysis.

Standard	Remarks
Fe	FeS <sub>2</sub> compound
Cr	Cr <sub>2</sub> O <sub>3</sub> compound
Mn	Pure element
Mo	Pure element
Ni	Pure element
Nb	Nb <sub>2</sub> O <sub>5</sub> compound
Si	SiO <sub>2</sub> compound
Ta	Pure element
V	V <sub>2</sub> O <sub>5</sub>
W	Measured from refractory element bar on diffusion couple (not available on standard block)

Light elements such as carbon, phosphorus, and sulfur were excluded from EDS quantification as they represented minimal amounts (less than 0.2 wt%) in the alloys and are not well measured using the EDS approach.

**c. Processing the Spectra of the Standards and Specimen to Remove the Background from the X-ray Peaks, so that the Measured Intensities Consist only of the Characteristic Signal**

Each standard was measured under uniform conditions, and the background removal was performed using EDAX Genesis software, an example of which can be seen in Figures 19 and 20.

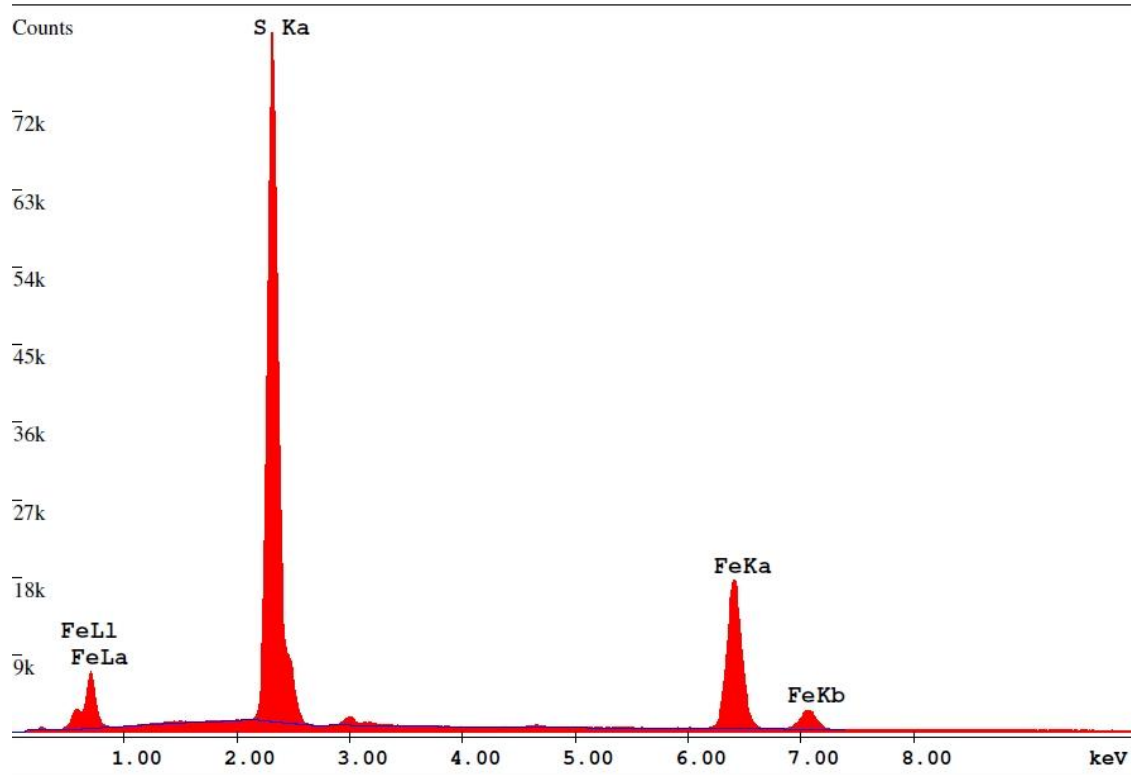


Figure 19. EDS spectrum for  $\text{FeS}_2$  pure standard.

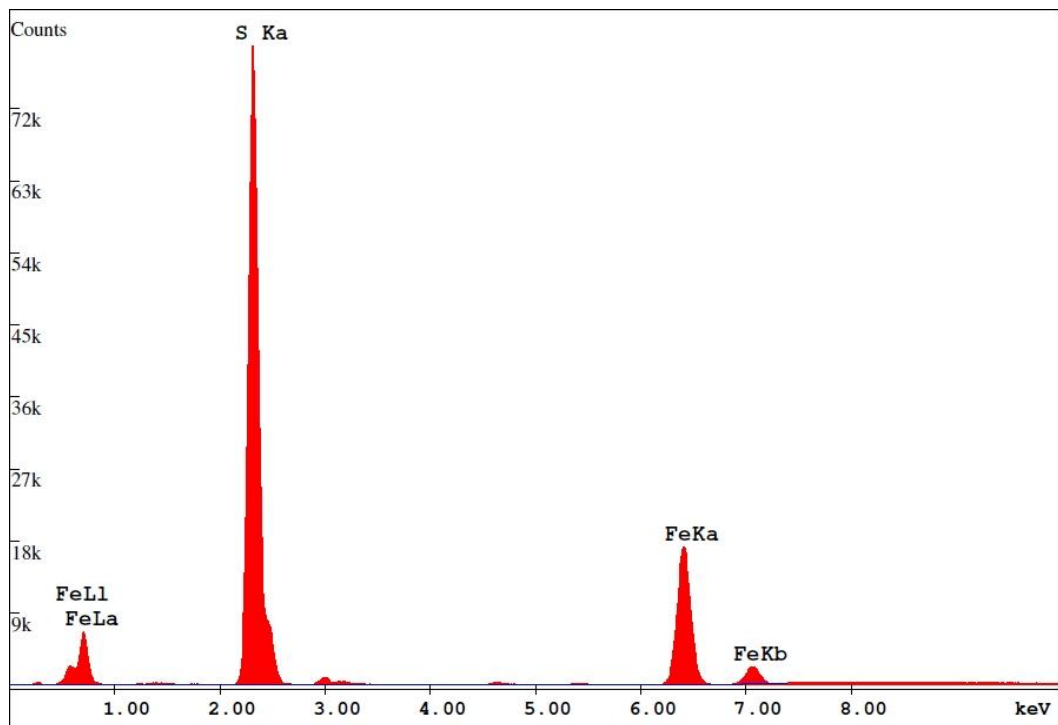


Figure 20. EDS spectrum for  $\text{FeS}_2$  pure standard with background subtracted.

*d. Developing the X-ray Intensity Ratios using the Specimen Intensity  $I_i$  and the Standard Intensity  $I_{(i)}$  for Each Element Present in the Sample and Carrying out Matrix Corrections to Obtain Quantitative Concentration Values.*

In order to quantify each diffusion couple (specimen) sample point, a table of standard intensities was systematically constructed:

Table 8. Calculated Pure Element Intensities ( $I_{(i)}$ )

Standard(with electron shell)	Intensity, $I_{(i)}$ (Counts)
<b>Fe-K</b>	4905.63
<b>Cr-K</b>	6588.89
<b>Mn-K</b>	5935.72
<b>Mo-L</b>	7029.21
<b>Ni-K</b>	3664.99
<b>Nb-L</b>	7280.25
<b>Si-K</b>	19199.88
<b>Ta-M</b>	6358.77
<b>V-K</b>	13780.59
<b>W-M</b>	6407.91

These intensities were used in conjunction with the EDAX Genesis software in the form of the ZAF matrix correction equation [22]:

$$\frac{C_i}{C_{(i)}} = [ZAF]_i \frac{I_i}{I_{(i)}} = [ZAF]_i k_i \quad (1)$$

$C_i$  = weight fraction of the element  $i$  of interest in the sample

$C_{(i)}$  = weight fraction of the element  $i$  in the standard

$\frac{I_i}{I_{(i)}}$  = ratio of the unknown-to-standard intensities, also known as the “k-value”

$[ZAF]_i$  = matrix effects correction factor due to atomic number (Z), x-ray absorption (A), and x-ray fluorescence (F), which varies by element.

Specimen spectra were obtained at individual points in a straight line away from the diffusion couple interface, perpendicular to the refractory element bar. Analysis point spacing of 5  $\mu\text{m}$  was chosen in order to correlate with the nanoindentation spacing (see section II.C for a more detailed discussion for this parameter). Analysis point locations varied based on the particular diffusion couple due to the differing diffusivities of each refractory element, as shown in Table 9.

Table 9. EDS Specimen sample ranges for each diffusion couple

Diffusion Couple	Analysis Range (distance from interface), $\mu\text{m}$	Total Analysis Points
Mo/316SS	0–100	20
Nb/316SS	5–200	13
Ta/316SS	5–120	12
W/316SS	5–300	21
Mo/HT9	390–785	32
Ta/HT9	0–200	14
W/HT9	200–600	33

Finally, the weight fractions for each element in the specimen sample point ( $C_i$ ) were calculated and tabulated.

#### 4. Calculation of “Effective” Diffusion Constants

Once EDS spectra were obtained for the diffusion couples, the compositional profiles of each refractory element were used to calculate an “effective” diffusivity for

the refractory elements in their respective alloy. For the sake of a simplified quantitative analysis, the diffusion couple specimens were modeled using the thin-film solution to the diffusion equation [23]:

$$C(x, t) = \frac{N}{\sqrt{4\pi Dt}} e^{-x^2/(4Dt)} \quad (2)$$

$C(x, t)$  = concentration (wt%) of refractory element at a given position  $x$  from the “film” (taken from experimental data).

$N$  = number of atoms per unit area initially placed at the film ( $x=0$ )

$D$  = diffusion constant [ $\text{cm}^2/\text{sec}$ ]

$t$  = time [sec]

For the diffusivity calculation, the “film” represented the diffusion couple interface where there was a high concentration of refractory element. In samples with the presence of multi-phase regions far from the interface (i.e., Mo/HT9 and W/HT9 samples), the film (or  $x=0$ ) location was chosen where the concentration of refractory element began to decrease.

Diffusivity can be found by linear-fitting a plot of  $\ln(C)$  versus  $x^2$  to find the slope,  $m$ , as shown in Figure 21. This slope is then defined via Equation (2) as

$$m = -\frac{1}{4Dt} \quad (3)$$

which can be rearranged to solve for diffusivity,  $D$ .

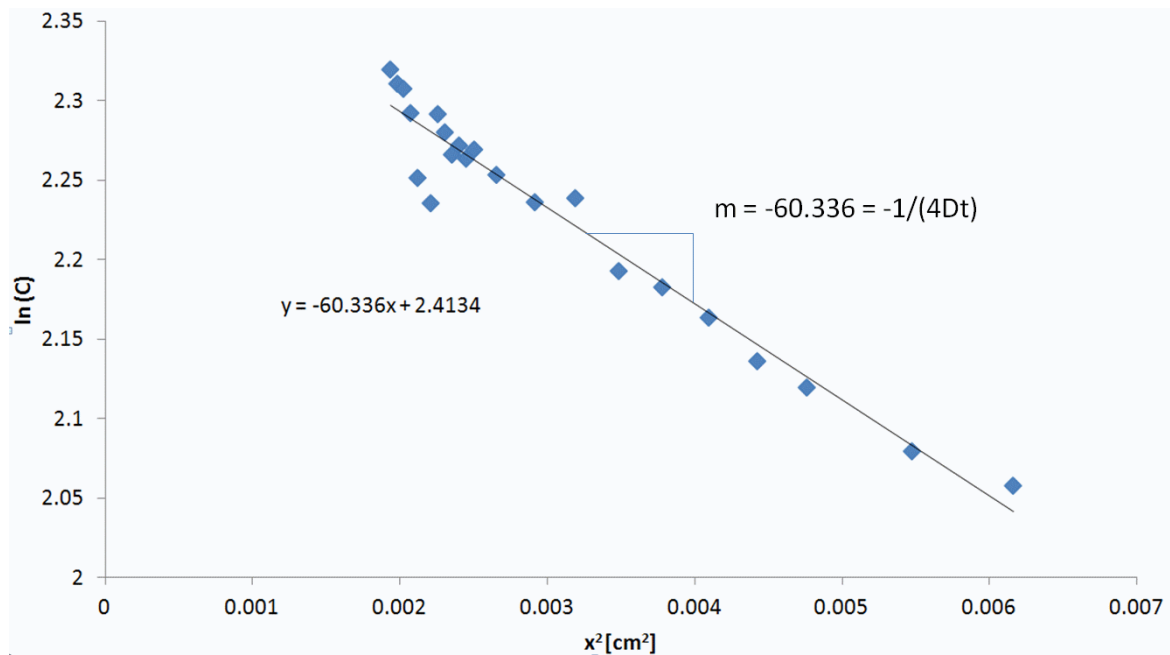


Figure 21. Log plot of concentration  $C(x,t)$  versus  $x^2$  for Mo/HT9 sample.

## C. NANOINDENTATION

### 1. Equipment

Nanoindentation was conducted at Naval Postgraduate School, Monterey on an Agilent G200 Nanoindenter (shown in Figure 22) utilizing a Berkovich diamond indenter tip. Agilent Nanosuite software was used for indentation data analysis and compilation.

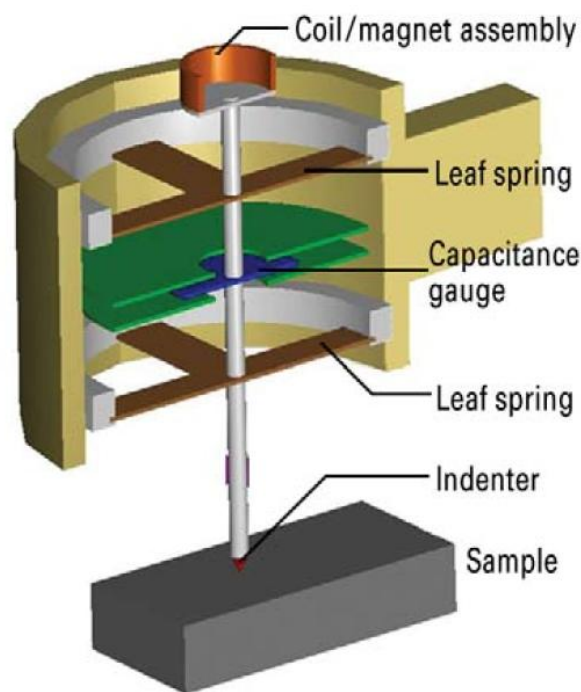
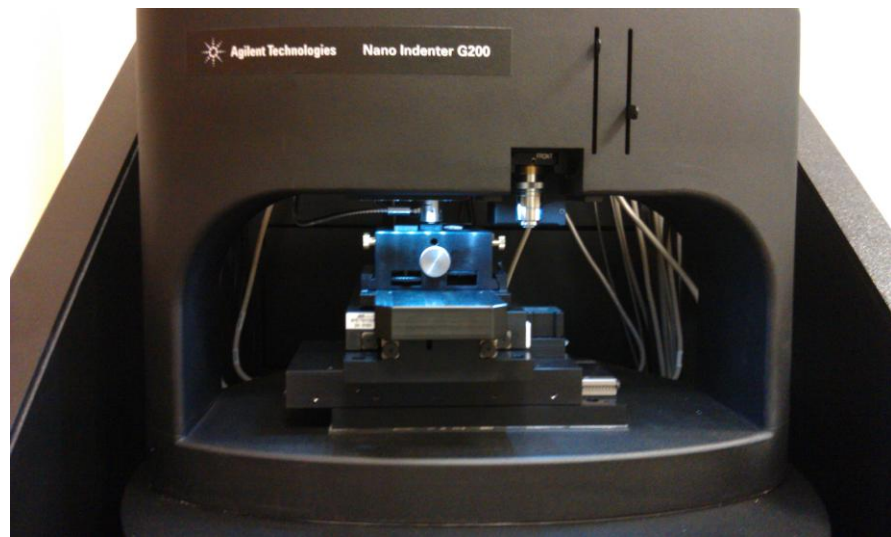


Figure 22. (Top) Agilent G200 Nanoindenter. (Bottom) Indenter column schematic (From [24]).

## 2. Assumptions

The focus of the nanoindentation phase was to attain representative hardness and elastic modulus data for sample points relatively close (<1mm) to the diffusion couple

interface. These results would then be coupled with the quantitative EDS composition to correlate refractory element composition with hardness and elastic modulus.

Utilizing the assumption of 1-D diffusion (and thus constant composition as a function of position), nanoindentation was performed in an array of  $3 \times n$  indents where  $n$  represents the number of analysis point columns spaced incrementally away from the interface. The average of the 3 rows would be used in determining the hardness and elastic modulus of the sample point; Figure 23 shows an example for the Ta/316SS diffusion couple.

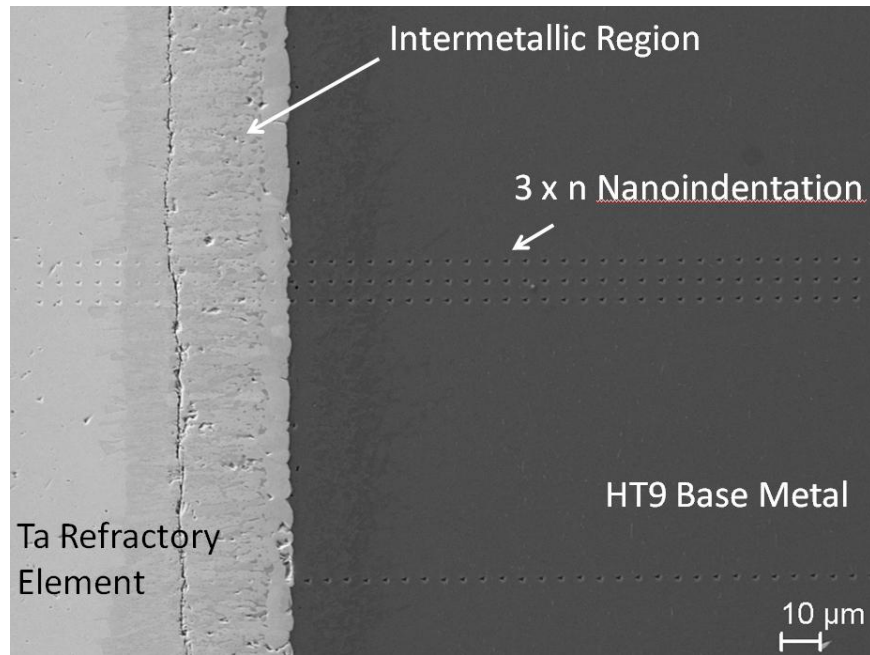


Figure 23.  $3 \times n$  indentation sequence for the Ta/316SS diffusion couple.

For a Berkovich tip, the width-to-depth ratio for an indentation is approximately 7:1. In general, the deeper the indentation, the more reliable the data becomes due to noise and surface effects at shallow indentation depths. Thus, it is necessary to strike a balance between achieving maximum spatial resolution of samples, while minimizing the interaction of overlapping stress fields from neighboring indents. Zhao suggests indentations be spaced at least twice the width of indentation apart [20]. For these experiments, an indentation depth of 200 nm was chosen with an associated spacing of 5  $\mu\text{m}$  between indents.

### 3. Experimental Procedure and Parameters

All specimen indentations were performed using the G200 XP indenter head via Continuous Stiffness Measurement (CSM). Unlike conventional, quasi-static indentation methods; where the stiffness is measured on the unloading of the indentation, CSM allows the ability to dynamically measure contact stiffness (and thus measure hardness and modulus) as a function of depth. This measurement is accomplished by superimposing an oscillatory harmonic load over the static load during indentation, thus eliminating the need to unload several times to measure properties as a function of indentation depth [25].

For this research, an indentation depth range of 100–190 nm was used to average values of hardness and modulus. This range was chosen from experience in using the Berkovich tip on metals where data at depth less than ~70 nm tended to be noisy. Between 100–190 nm indentation depth range, the rate of change of properties is minimal, as shown in Figure 24.

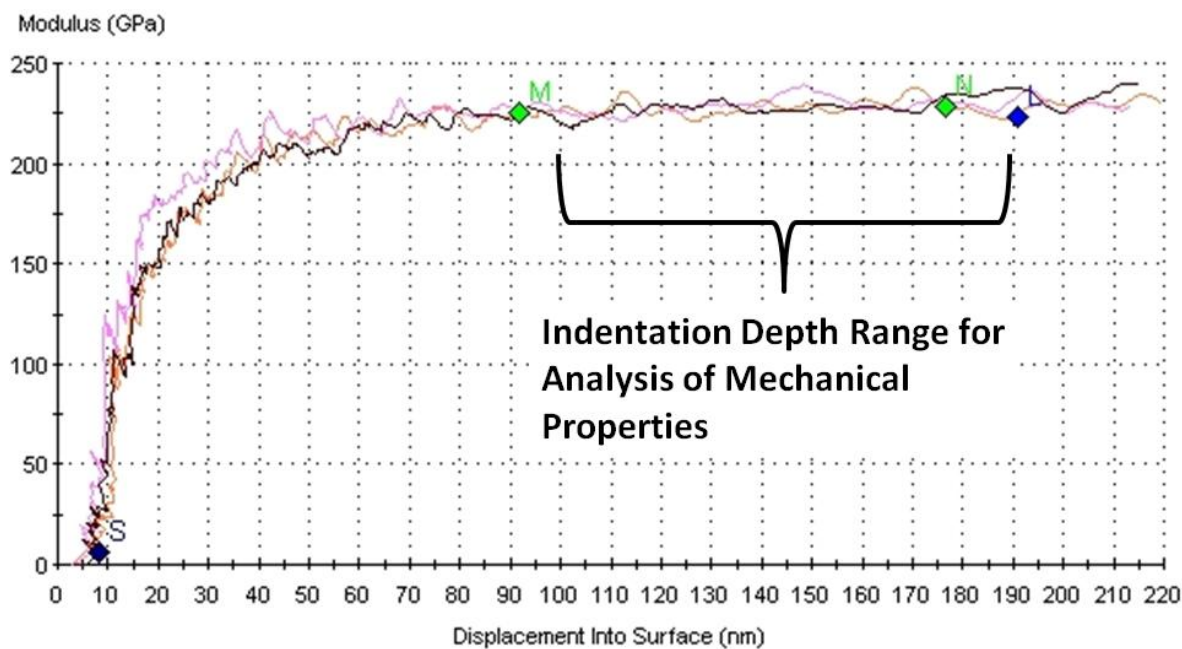


Figure 24. Plot of modulus vs. indentation depth for 3 indentations, Mo/316SS sample.

Prior to indentation, tip calibration was performed on fused silica to determine the indenter tip area function. The remaining input parameters used in the specimen CSM measurements as recommended by Hay and Agee are listed in Table 10 as follows [25]:

Table 10. CSM method nanoindentation parameters.

Parameter	Value
<b>Berkovitch tip serial number</b>	TB15658
<b>x-spacing</b>	5 $\mu\text{m}$
<b>y-spacing</b>	5 $\mu\text{m}$
<b>Surface approach distance</b>	1000 nm
<b>Surface approach speed</b>	10 nm/sec
<b>Surface detect stiffness criteria</b>	200 N/m
<b>Indent depth limit</b>	200 nm
<b>Poisson's ratio</b>	0.3
<b>Maximum drift rate</b>	0.015 nm/sec
<b>Strain rate target</b>	0.05 $\text{s}^{-1}$
<b>CSM harmonic displacement</b>	2 nm
<b>CSM harmonic frequency</b>	45 Hz
<b>Maximum drift delay time</b>	6 hrs

THIS PAGE INTENTIONALLY LEFT BLANK

### III. RESULTS AND DISCUSSION

#### A. OPTICAL MICROSCOPY

Diffusion couple specimens were examined under the optical microscope to assess the amount of bonding between the refractory element and base metal (Figures 25 and 26).

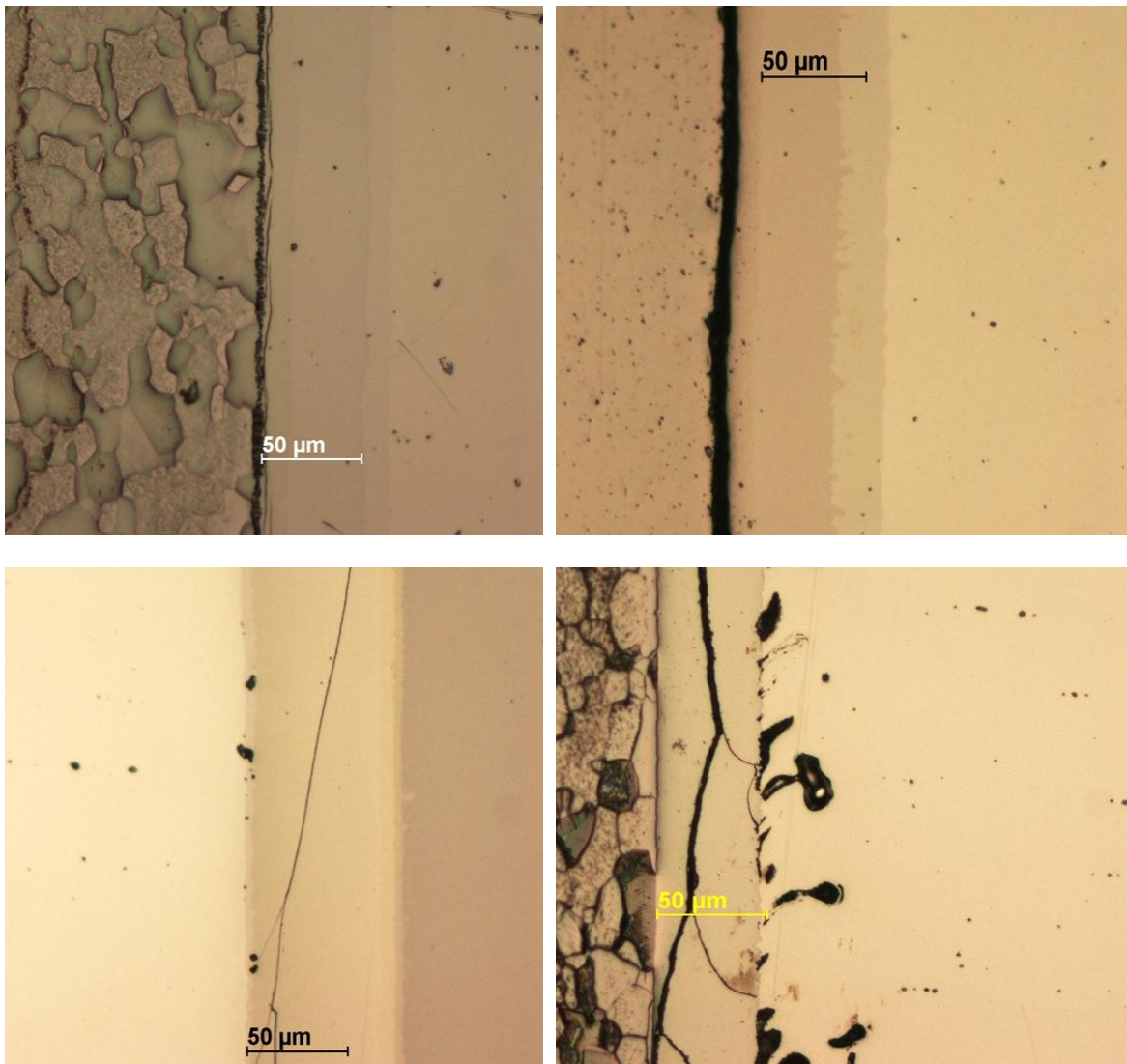


Figure 25. Optical microscopy images of 316SS diffusion couple specimens. Top left: molybdenum; top right: niobium; bottom left: tantalum; bottom right: tungsten. All images are oriented with the refractory element on the left side and base metal on the right.

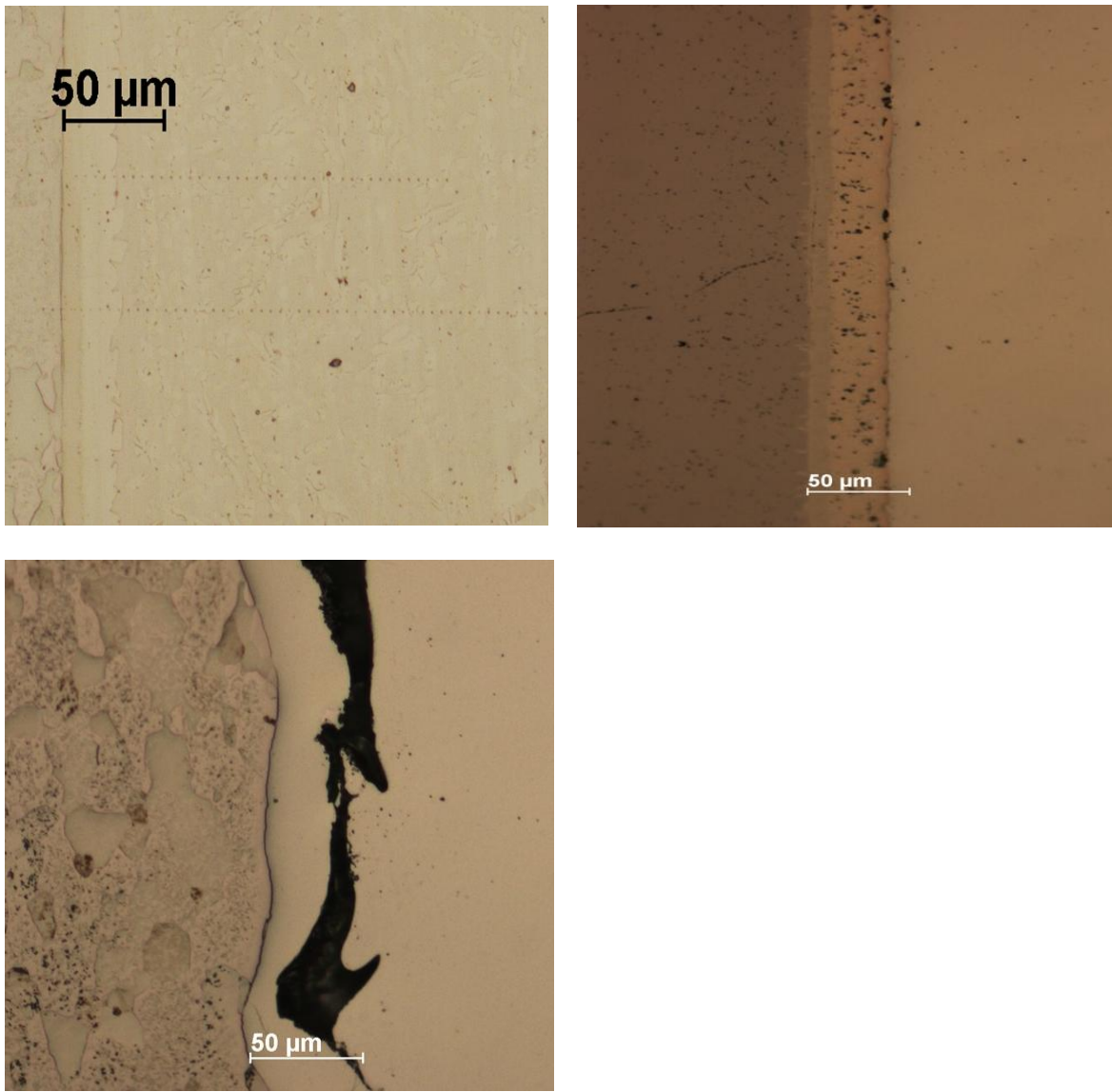


Figure 26. Optical microscopy images of HT9 diffusion couple specimens. Top left: molybdenum; top right: tantalum; bottom left: tungsten. All images are oriented with the refractory element on the left side and base metal on the right.

Optical microscopy confirmed satisfactory contact between in all samples with the exception of the W/316SS and W/HT9 diffusion couples. Tungsten specimens showed extensive cracking and separation at the interface; however, quantitative EDS results confirmed that this most likely occurred after the HIP process, as inter-diffusion was later confirmed by the presence of substantial tungsten in the base metal.

Optical images of Mo/HT9 sample revealed an extensive, dual-phase region present as far as 400  $\mu\text{m}$  from the interface as seen in Figure 27. EDS later confirmed that these formations were molybdenum-rich intermetallic, phases.

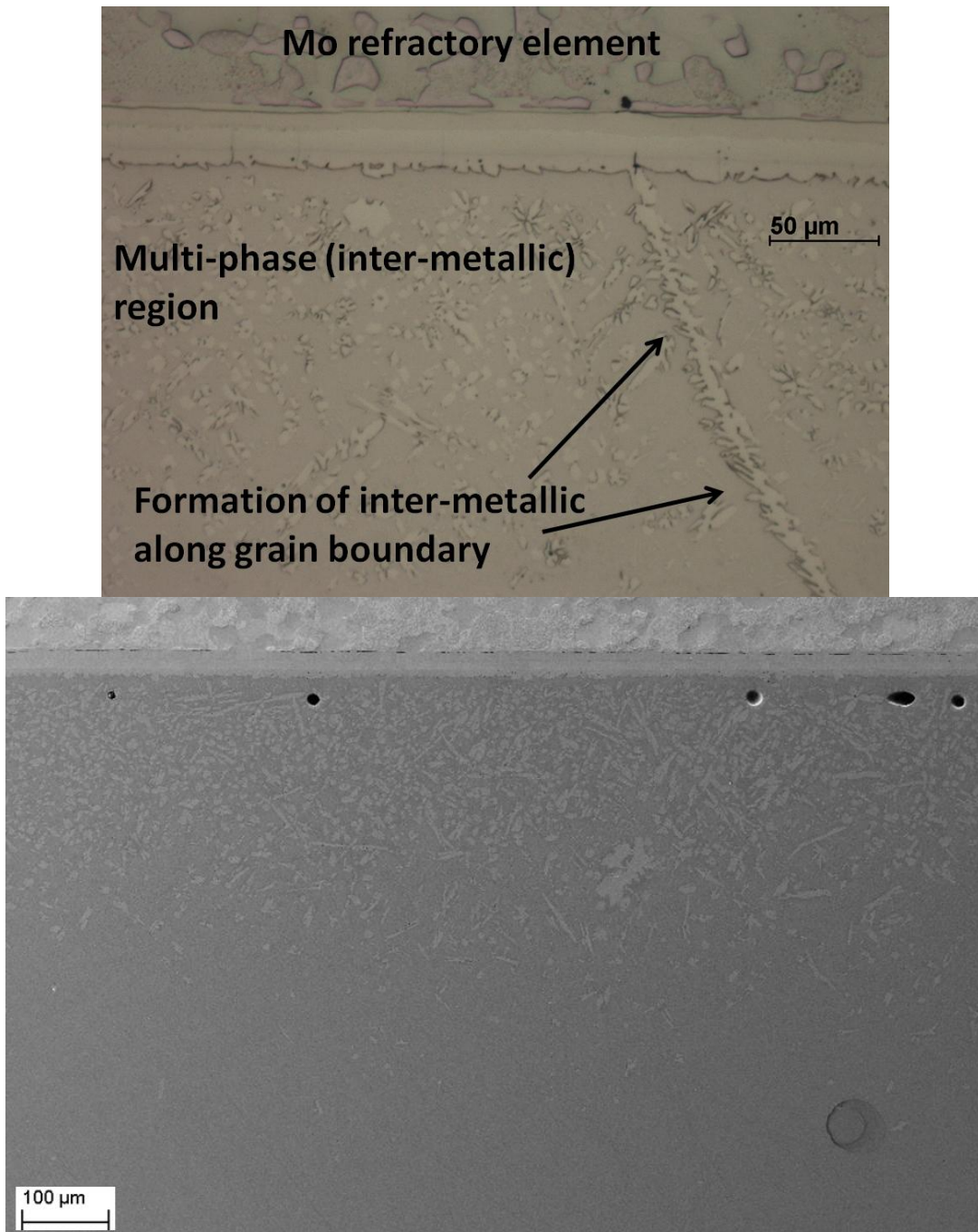


Figure 27. (Top) Optical image of Mo/HT9 sample showing inter-metallic phase formations; (Bottom) SEM image of Mo/HT9 sample showing the extent of formation.

## B. MATERIAL CHARACTERIZATION

### 1. Refractory Element Composition versus Position

EDS spectra were obtained at multiple points away from the inter-metallurgical interface for each sample in weight percent composition. Plots of composition versus position can be seen in Figure 29. For comparison, a typical EDS spectrum near the interface and far from the interface are overlaid in Figure 29. In this figure, a large MoLa peak is visible in the spectrum near the interface, signifying the substantial diffusion of molybdenum into the material at the interface. It should be noted that even far from the interface, there is still a measurable amount of molybdenum in the steel which is in line with the base composition of 316SS, 2–3wt%.

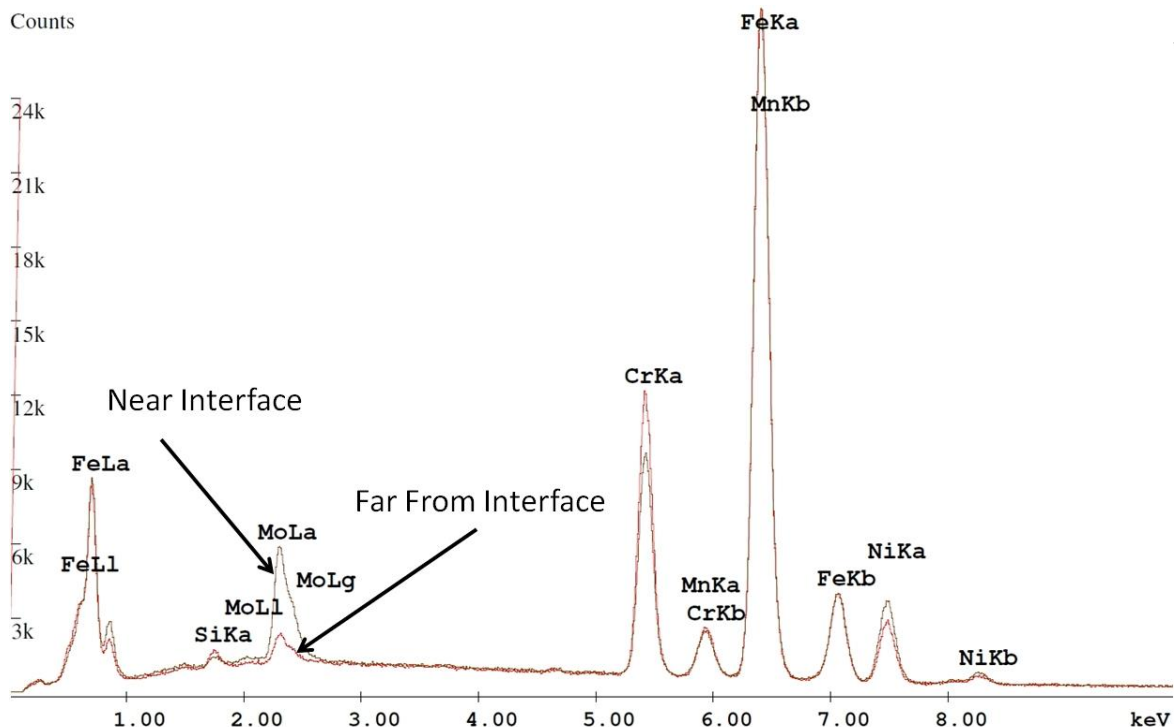


Figure 28. Overlaid EDS spectra near and far away from the diffusion couple interface for Mo/316SS sample.

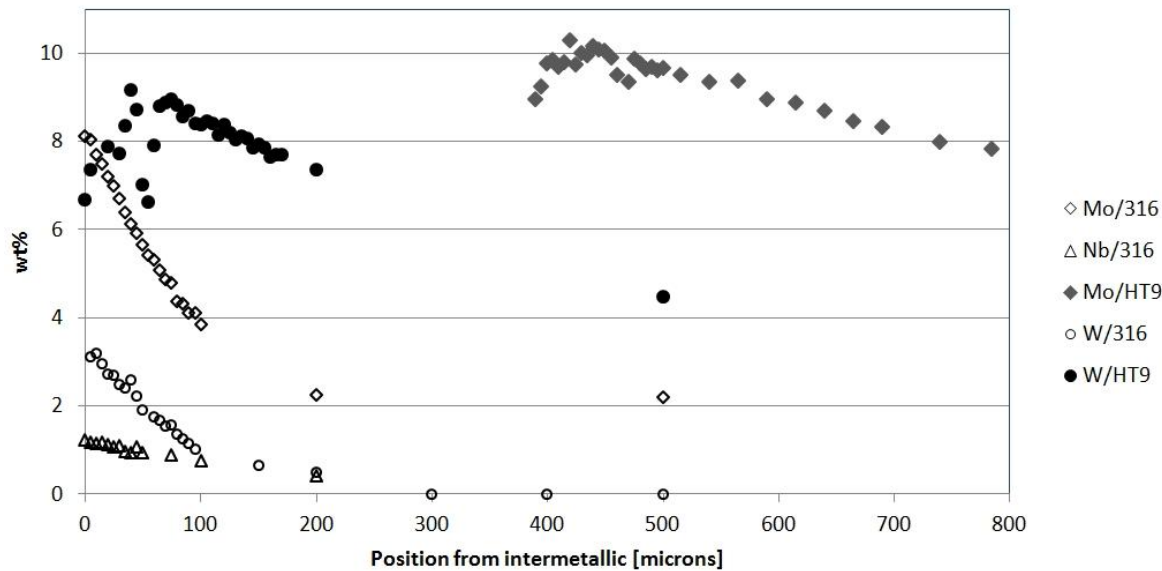


Figure 29. Plots of weight percent versus position from interface for 316SS and HT9 diffusion couples.

Note that plots of Ta composition for 316SS and HT9 samples are not shown, as there was no appreciable diffusion of tantalum into either diffusion couple. In the case of the Mo/HT9 and W/HT9 samples, quantitative EDS was performed farther away from the diffusion couple interfaces due to the evidence of dual-phase regions extending as far out at 400  $\mu\text{m}$  from the refractory element interface (Figure 30). The composition of the steel phase should not vary in a two phase region, but the apparent composition may change due to interaction between the analysis volume and intermetallic phases.

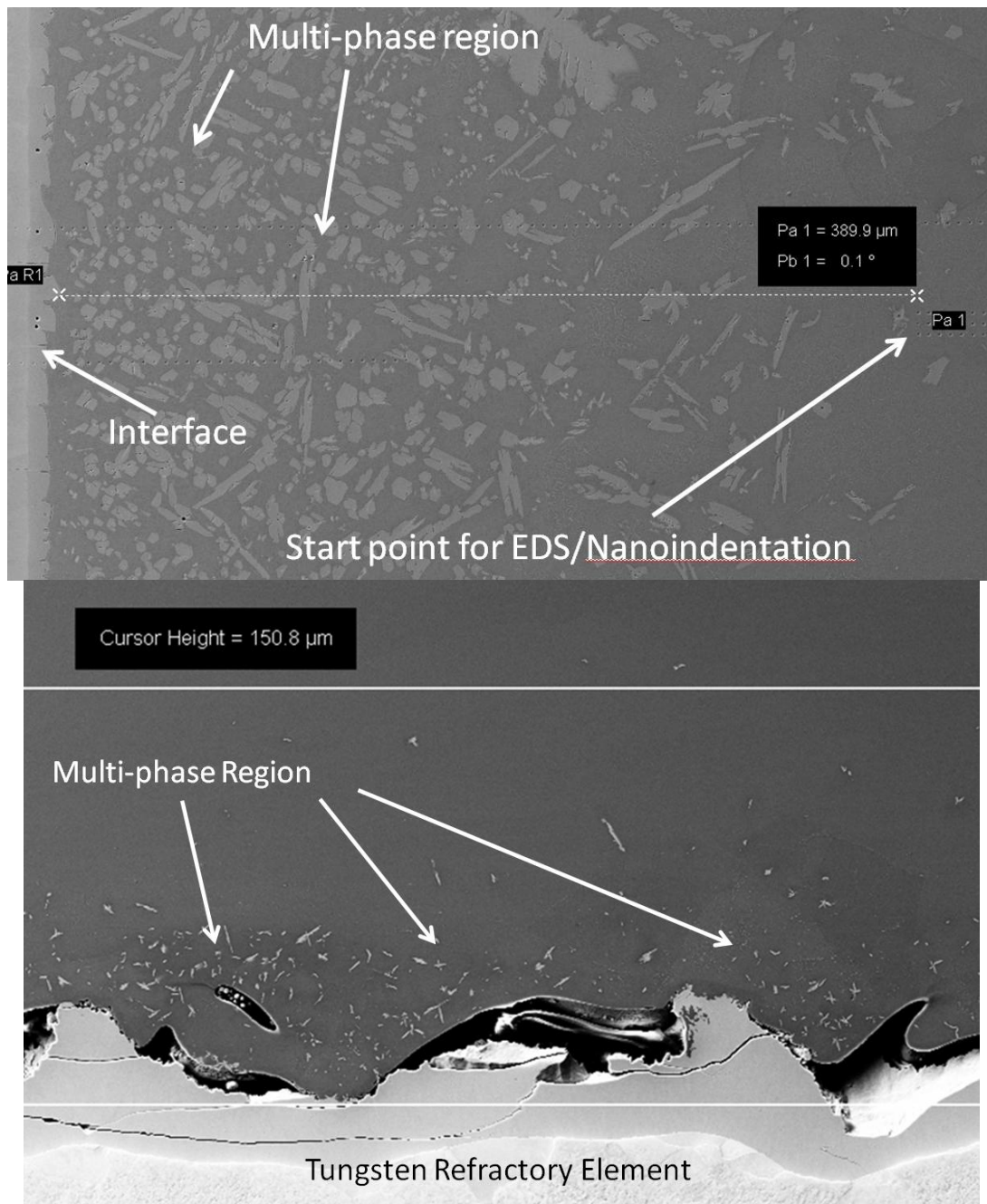


Figure 30. SEM Image of multi-phase regions in (Top) Mo/HT9 sample, (Bottom) W/HT9 sample

EDS quantification of the lighter contrast, dual-phase formations on the Mo/HT9 sample in Figure 30 revealed the following composition:

Table 11. Composition (in wt%) of dual-phase formations in Mo/HT9 sample.

<b>SiK</b>	<b>MoL</b>	<b>CrK</b>	<b>MnK</b>	<b>FeK</b>	<b>NiK</b>
0.69	24.69	13.12	0.54	59.84	1.11

## 2. “Effective” Diffusion Constants

Diffusion constants were calculated using Equation (3). Values of  $C(x,t)$  were obtained by quantitative EDS. The diffusion constants for the Ta/316 and Ta/HT9 samples were not calculated as no measurable diffusion of tantalum into steel was observed. The measured diffusivities are summarized in Table 12. Results revealed that alloy HT9 measured diffusivities were over an order of magnitude larger than those of alloy 316. No diffusivity was calculated for the Ta-based diffusion couples as there was no measurable level of Ta in the steels.

Table 12. Calculated “Effective” diffusivity for refractory elements into their respective alloys.

<b>Diffusivity</b>	<b>Calculated Value [cm<sup>2</sup>/sec]</b>	<b>Effective “film” distance from interface [μm]</b>
$D_{Mo-316SS}$	$5.588 \times 10^{-11}$	0
$D_{Nb-316SS}$	$6.854 \times 10^{-11}$	0
$D_{Ta-316SS}$	-	N/A
$D_{W-316SS}$	$3.602 \times 10^{-11}$	0
$D_{Mo-HT9}$	$2.877 \times 10^{-9}$	440
$D_{Ta-HT9}$	-	N/A
$D_{W-HT9}$	$1.319 \times 10^{-9}$	0

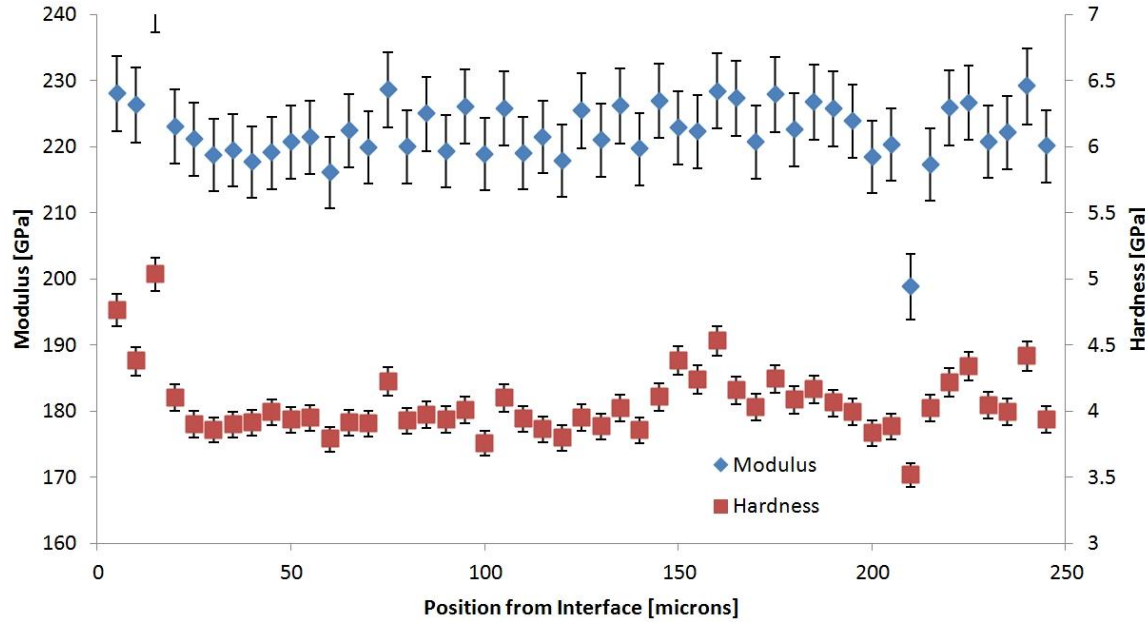
## 3. Nanoindentation

Values of hardness and elastic modulus were obtained and are shown in Figures 31 and 32. For each of the plots, the magnitude of hardness and Young’s modulus scales were preserved to show the relative change in properties between samples.

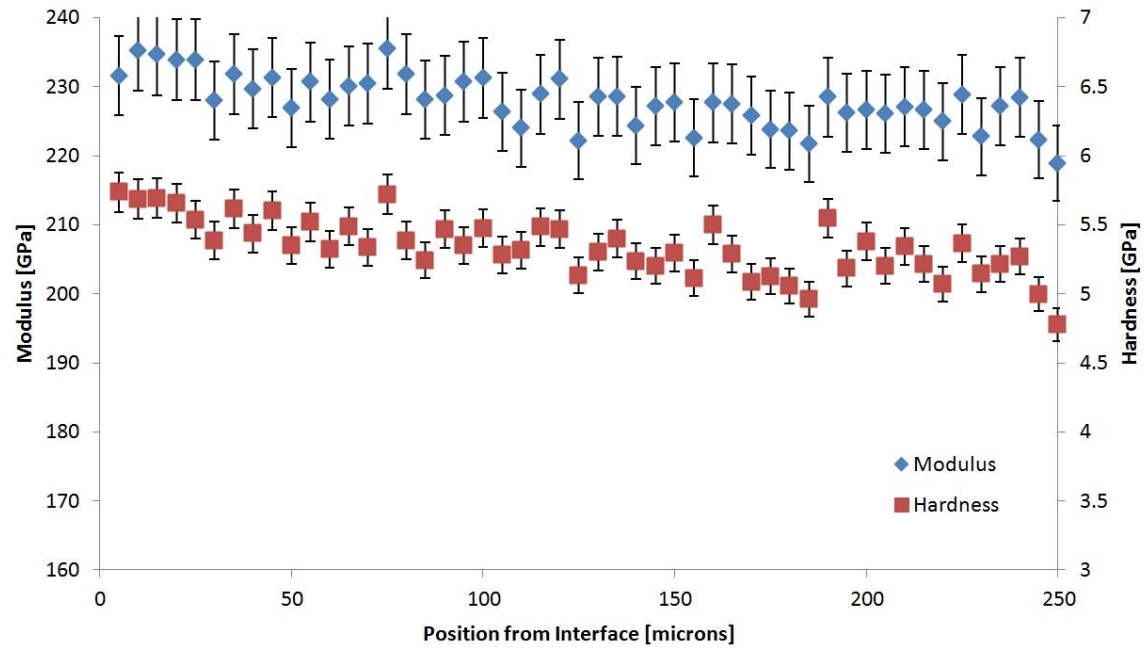
A sensitivity analysis was performed on the nanoindentation results to examine the magnitude in error for hardness and Young’s modulus. Standard deviation was calculated using the Ta/316 and Ta/HT9 mean measured properties far from the interface (since these samples were least likely to be affected by any appreciable refractory

element). In both cases, standard deviation for hardness and Young's modulus was no higher than 2.07%. Thus, for plotting purposes, an error of 2.5% was applied to the plotted points.

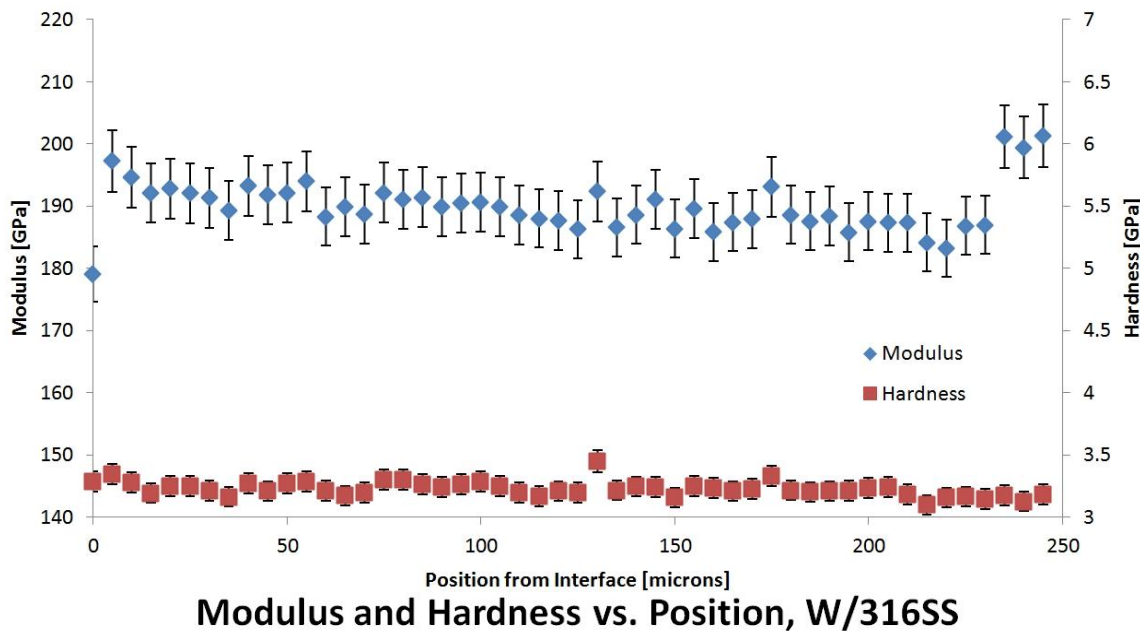
### Elastic Modulus and Hardness vs. Position, Mo/316SS



### Modulus and Hardness vs. Position, Nb/316SS



### Modulus and Hardness vs. Position, Ta/316SS



### Modulus and Hardness vs. Position, W/316SS

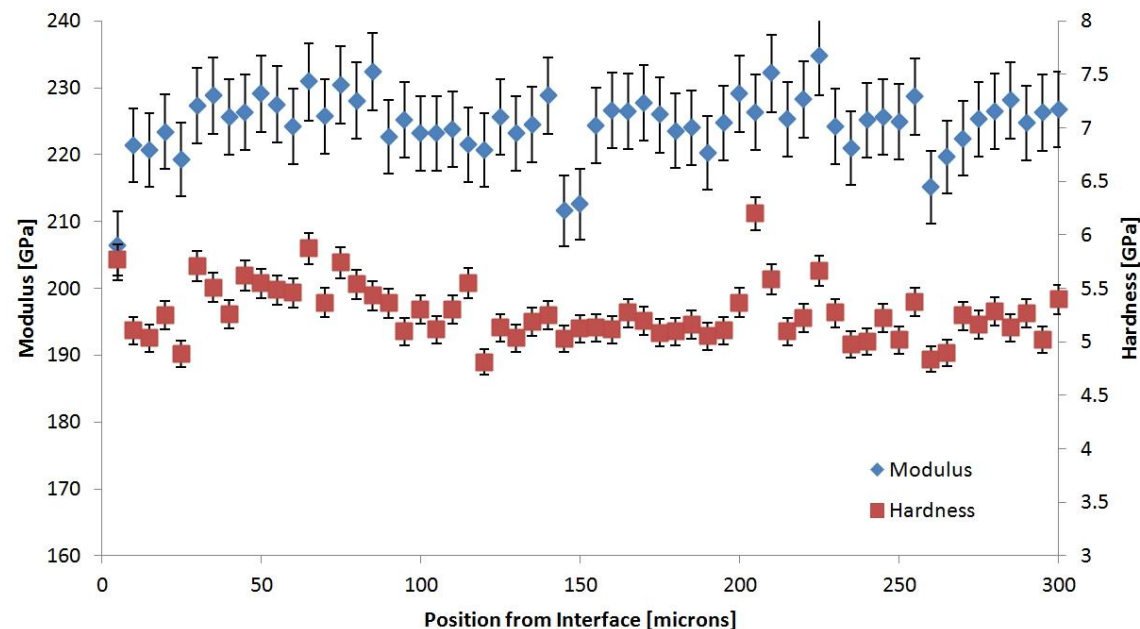
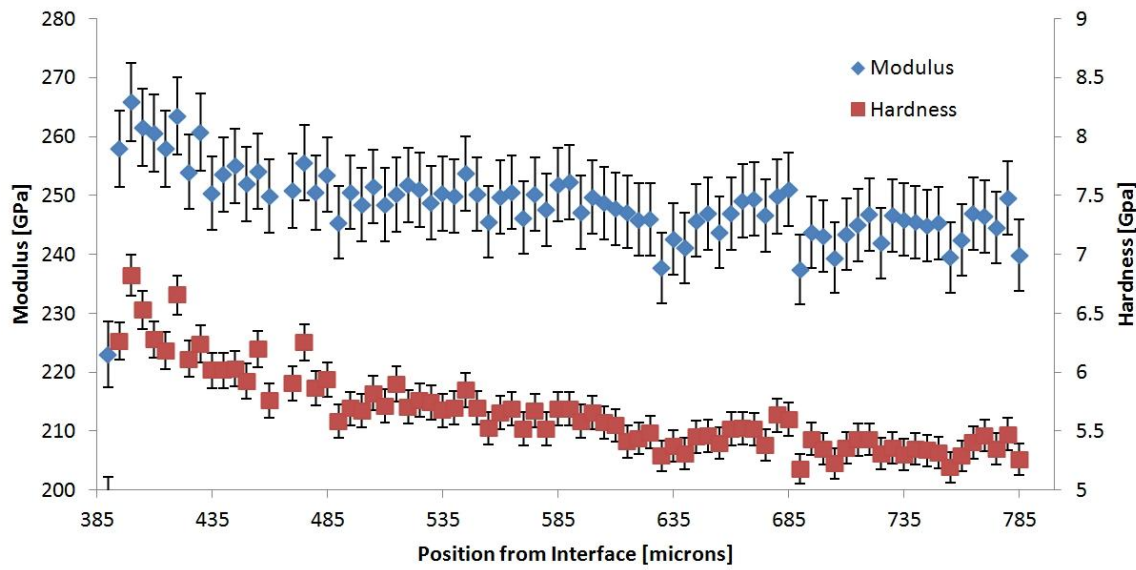
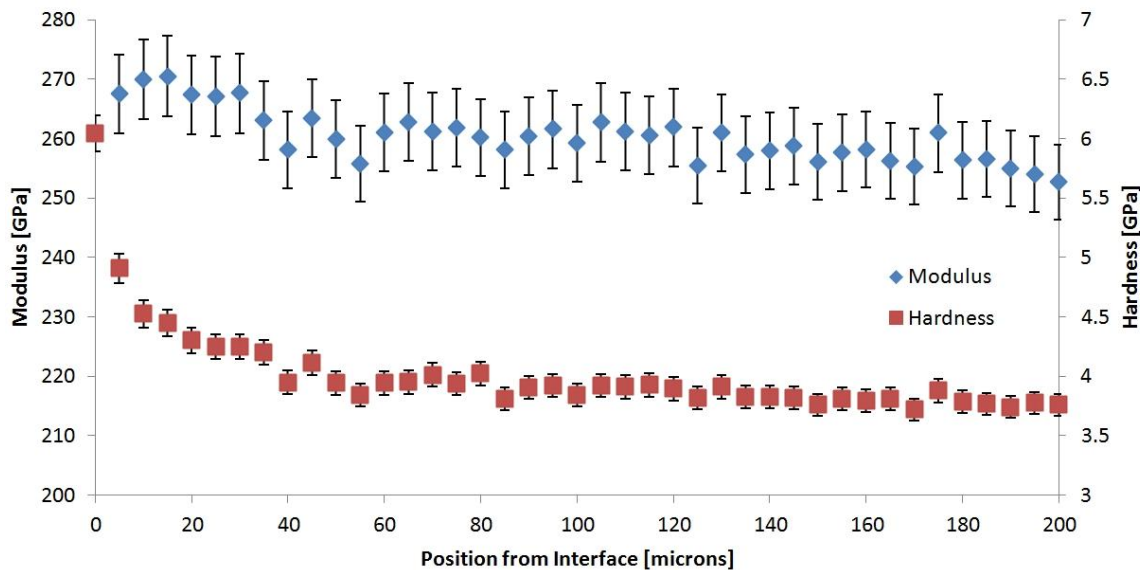


Figure 31. Plots of modulus and hardness vs. position from interface for 316SS diffusion couples.

### Hardness and Modulus vs. Position, Mo/HT9



### Modulus and Hardness vs. Position, Ta/HT9



## Modulus and Hardness vs. Position, W/HT9

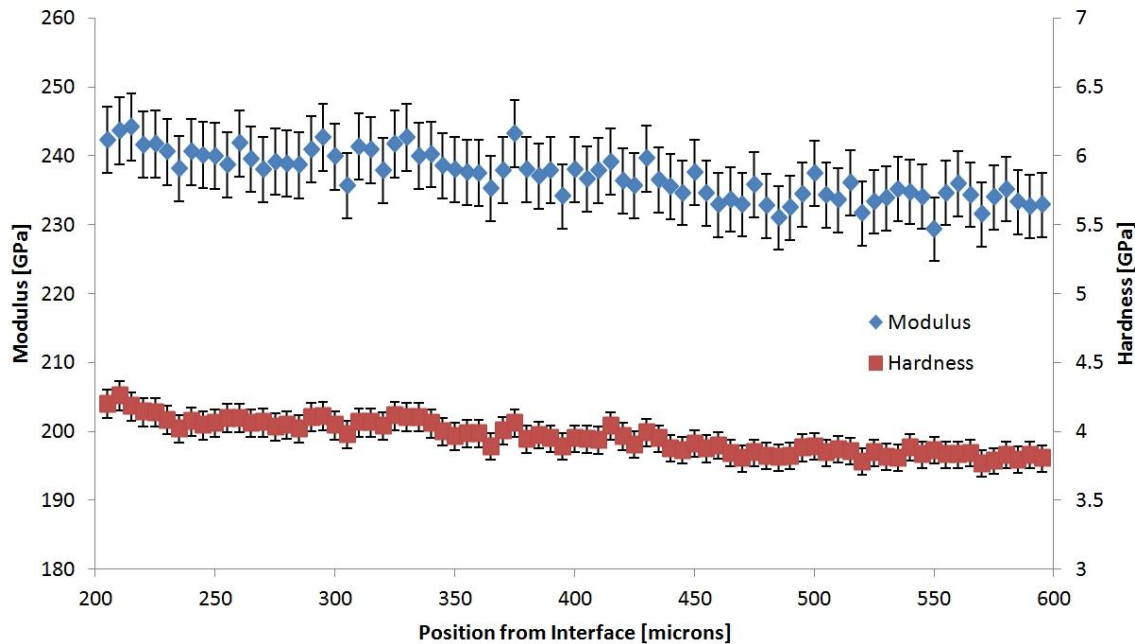


Figure 32. Plots of modulus and hardness vs. position from interface for HT9 diffusion couples.

Nanoindentation results showed the most notable rise in hardness and Young's modulus occurred in the HT9 diffusion couples. In the alloy 316SS diffusion couples, the only appreciable trend in hardness occurred in the Mo/316SS sample within 100 $\mu$ m of the interface.

### C. DISCUSSION: THESIS QUESTION REVISITATION

#### 1. What is the Maximum Amount of Refractory Element that can be Added in Each Alloy before the Solubility Limit is Reached?

All diffusion couples showed some level of solubility with the exception of tantalum in either alloy. Although optical micrographs showed good physical contact between the refractory element and the base metal for both the Ta/316 and Ta/HT9 samples, EDS could not measure a Ta signal above background using the pure standard and Ta-M line in either sample. This conclusion is supported by examining an overlay of EDS spectra in which little change observed in the Ta X-ray intensity peaks, as shown in Figure 33. For the HT9 sample, there is no observable difference at the tantalum M-line

near and far away from the interface. For the 316 SS sample, it is possible that there is some change in tantalum level, but it should be noted that tantalum and silicon have a strong peak overlap and that 316SS does contain some silicon (approximately 0.3 wt%).

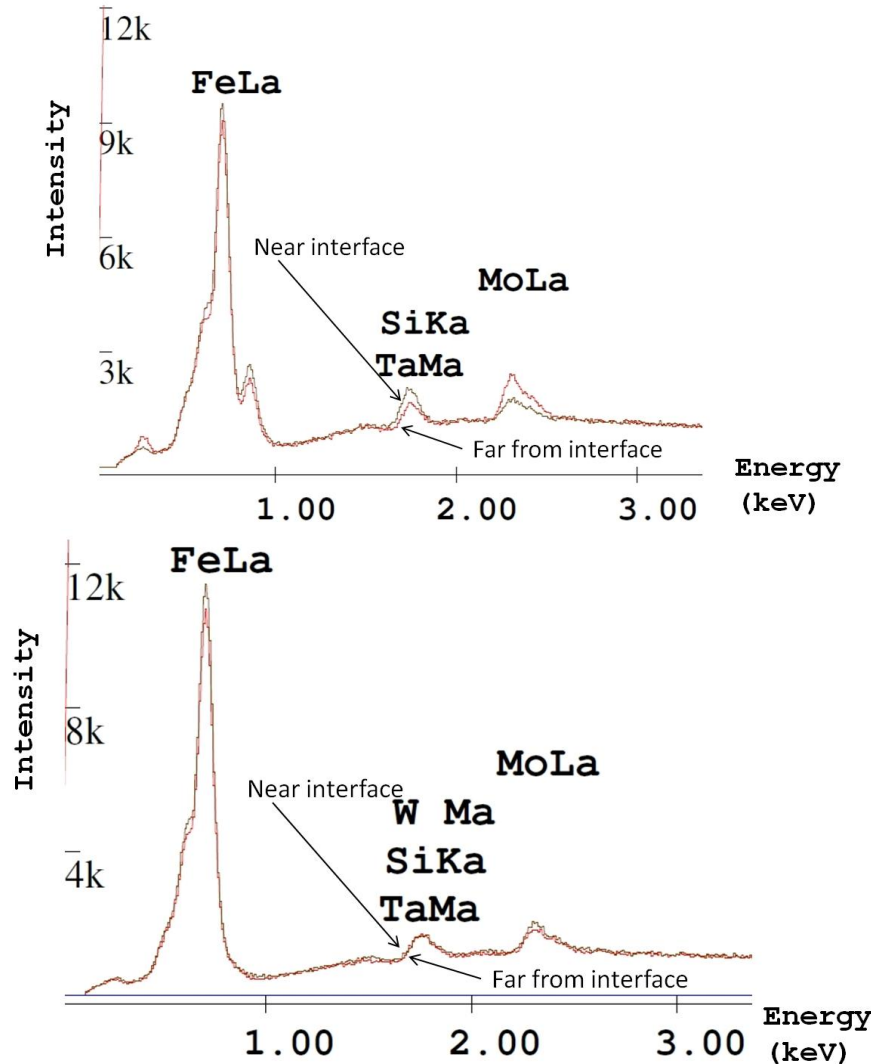


Figure 33. EDS overlay spectra for Ta/316 (top) and Ta/HT9 (bottom) diffusion couples

SEM images revealed microstructural changes near the diffusion couple interface for the Ta/HT9 sample, as seen in Figure 34. Additionally, nanoindentation results showed a rise in hardness with position approaching the interface. A hypothesis for this phenomenon is that despite observing little appreciable change in Ta composition in the base metal, there may be inter-granular diffusion of tantalum in amounts below the

sensitivity and resolution of EDS quantification which may cause the higher hardness near the inter-metallic interface. Electron backscatter diffraction (EBSD) measurement and transmission electron microscopy (TEM) would be needed to determine the exact mechanism of these microstructural changes.

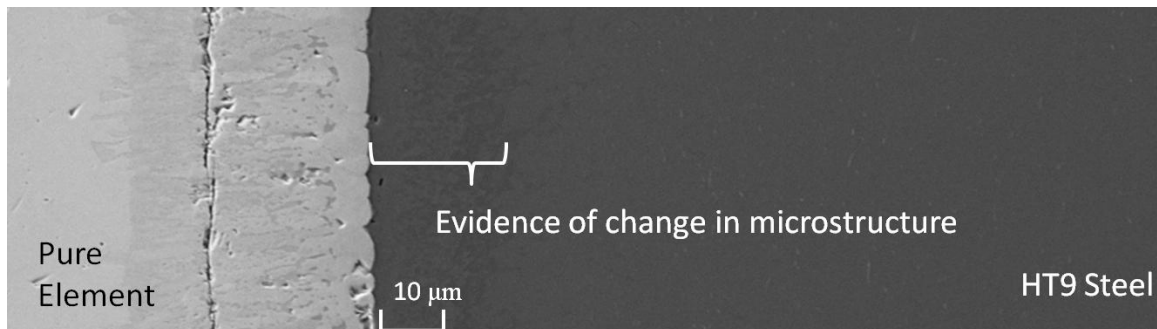


Figure 34. Micrograph image of Ta/HT9 sample, showing evidence of microstructural change near the interface.

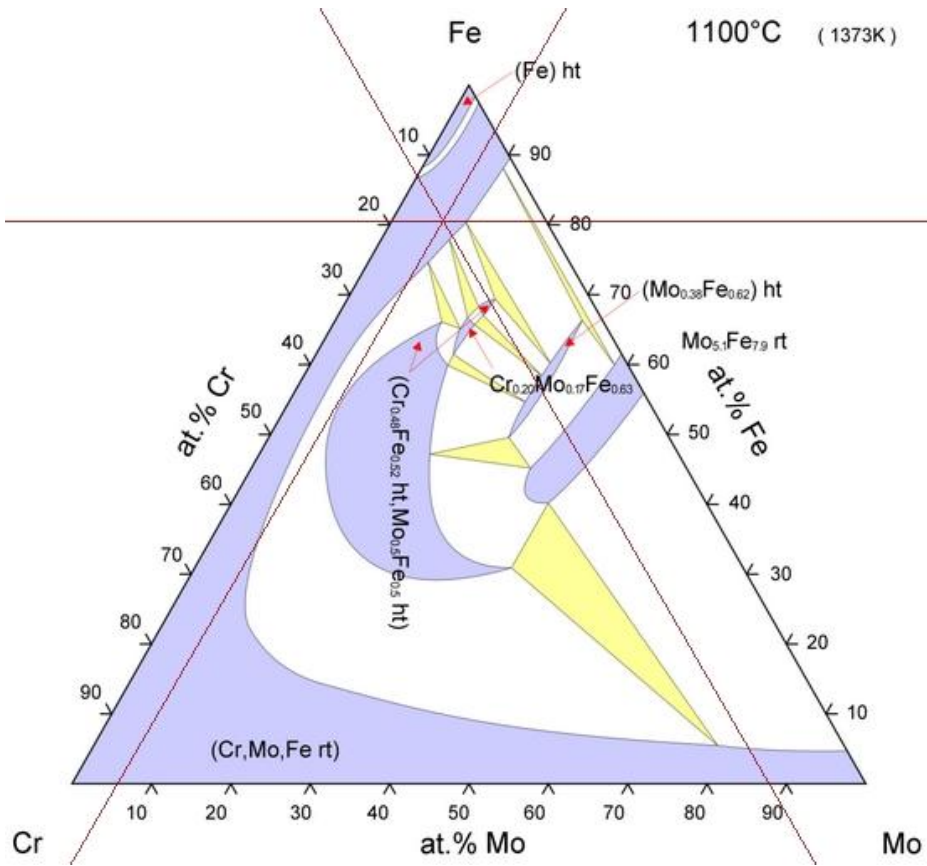
In comparing the relative solubilities of the refractory elements, it is useful to view compositional diffusion profiles with respect to position from the interface (with the exception of Ta in either alloy) shown in Figure 29.

From these profiles, one can estimate the approximate solubility at 1100 °C for Mo in 316SS and HT9, Nb in 316SS, and W in 316SS and HT9 from the peak compositions. It is vital to note that all diffusion in these samples took place at 1100 °C. The solubility at this high temperature is to be expected to be much larger than at lower temperatures. An obvious observation from the figure is that the solubility of Mo and W in HT9 is higher than that of alloy 316SS. The lower solubility in alloy 316SS is most likely due to the presence of Ni in the stainless steel, whereas the only major alloying element in HT9 is that of Cr. The solubility of the refractory elements is generally lower in the more tightly-pack FCC lattice of austenite and in the BCC lattice of ferrite, thus an austenite stabilizer, such as nickel, suppress the high temperature solubility of the large, refractory metal atoms.

Solute size undoubtedly plays a role in the relative solubility of the refractory elements in either alloy. The percentage of solute mismatch to iron, as seen in Table 4, is inversely proportional to the relative solubility as seen in the experimentally-determined

results. Tantalum, which has the highest solute mismatch, was the least soluble followed by niobium, which had a maximum composition just over 1 wt% in the alloy 316SS diffusion couple.

It is useful to compare ternary phase diagrams at 1100°C for each a refractory element in combination with Fe and Cr. Since compositions of Mo and W are appreciable in the two alloys, the ternary diagrams for these elements are a good benchmark for comparison against the experimental data. Unfortunately, there is little information regarding ternary phase diagrams for Nb and Ta in the literature, thus preventing the comparison of solubility with known phase diagrams. Shown in Figure 35 are ternary phase diagrams for Fe-Cr-Mo and Fe-Cr-W.



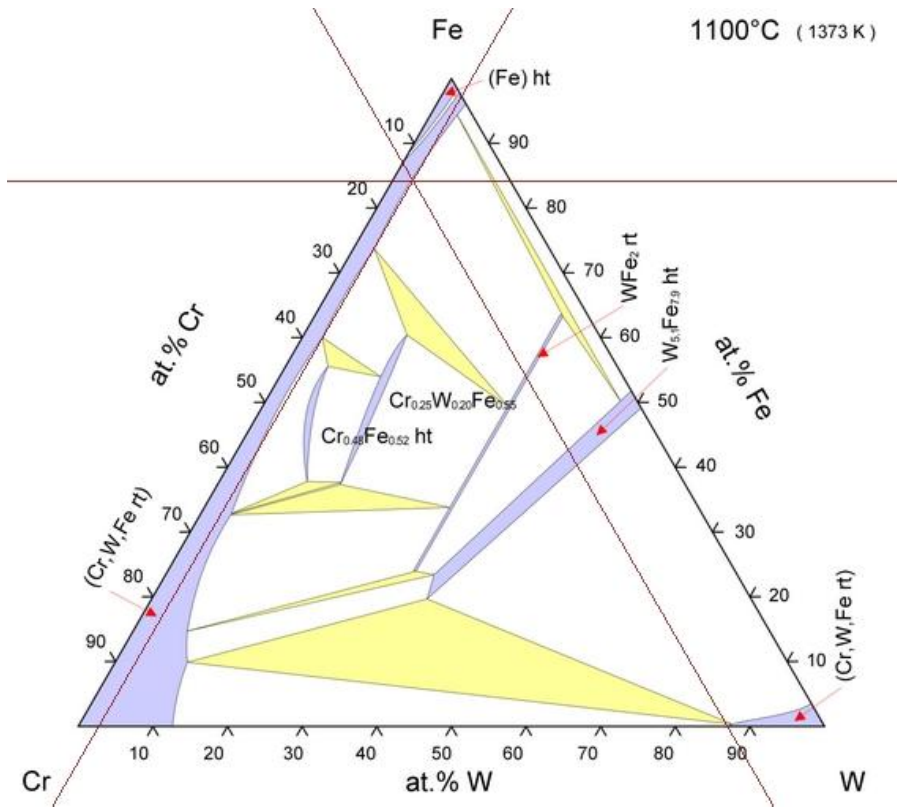


Figure 35. Ternary phase diagram for Fe-Cr-Mo (top), and Fe-Cr-W (bottom) (isothermal sections at 1100 °C). The intersection of the 3 lines shows the approximate compositions measured near the interface for the alloy HT9 diffusion couples. Blue regions in the diagram represent  $\alpha$ -ferrite phase, white regions represent dual-phase of ferrite/inter-metallic, and yellow regions are three-phase region of ferrite and two different inter-metallic phases (From [26]).

The ternary diagrams tend to match the approximate solubilities for the Mo and W in the alloy HT9 diffusion couples. Despite the fact that there are more than 3 elements in alloy HT9, the ternary phase diagram is a still good estimate of phase boundaries because of the small compositions of the remaining alloy additions (as seen in Table 3), and the fact that these alloys drive the phase stability toward a BCC crystal structure.

Estimating the solubility for the alloy 316SS with refractory additions is slightly more complex, since there are 4 major alloying elements in solution: Fe, Ni, Cr, and the refractory element. Predicting the phase stability requires the use of a quaternary phase

diagram. With molybdenum, however, it is possible to determine an “equivalent” concentration of Cr by way of the Shaeffler-DeLong equation [14]:

$$\% \text{Cr}_{\text{eq}} = \% \text{Cr} + \% \text{Mo} + 1.5(\% \text{Si}) + 0.5(\% \text{Nb}) \quad (\text{in wt\%}) \quad (4)$$

This can provide an approximation of the phase of the thermodynamic state to compare with the solubility measured in the Mo/316SS sample. Thus, for the EDS quantification at the interface where the composition was Fe-13.22Cr-12Ni-8.11Mo-0.3Si, the Shaeffler-DeLong Cr equivalent composition is 22 wt%. From here one can examine the ternary Fe-Cr-Ni phase diagram, as shown in Figure 36.

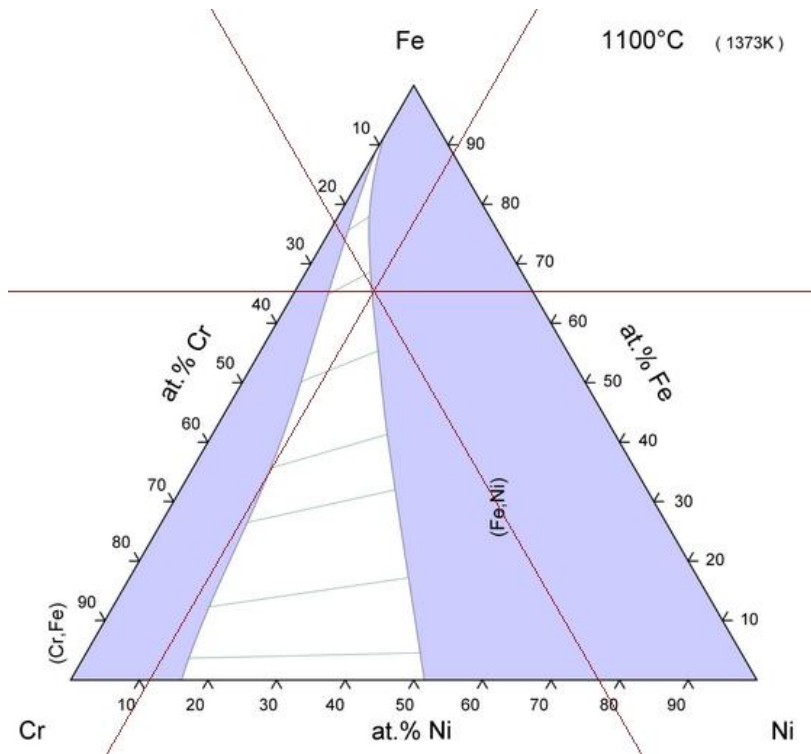


Figure 36. Fe-Cr-Ni ternary phase diagram showing the thermodynamic state at max solubility for Mo/316 sample based on the Shaeffler-DeLong equivalent Cr. The blue region to the right of the ternary diagram is  $\gamma$ -Fe phase (From [26]).

Thus, from the ternary diagram one can conclude that at 8 wt% Mo maximum solubility, the 316SS is most likely in the austenite phase at 1100 °C, but at the edge of the two-phase boundary between FCC and BCC crystal structure.

## 2. What is the Relative Diffusivity for Each Refractory Element in Alloy 316 and Alloy HT9?

The values of diffusivity measured in Table 12 match calculated diffusivities from previous publications on measured binary diffusivities of refractory elements in pure  $\gamma$ -Fe or  $\alpha$ -Fe, as shown in Table 13.

Table 13. Comparison of experimentally-determined diffusivities with those measured in previous works.

Diffusivity	Experimental Value [cm <sup>2</sup> /sec]	Value from Previous Work [cm <sup>2</sup> /sec]
$D_{Mo-316SS}$	$5.588 \times 10^{-11}$	$6.69 \times 10^{-11}$ (From [27])
$D_{Nb-316SS}$	$6.854 \times 10^{-11}$	$4.3948 \times 10^{-11}$ (From [28])
$D_{W-316SS}$	$3.602 \times 10^{-11}$	$3.5-4 \times 10^{-11}$ (From [29])
$D_{Mo-HT9}$	$2.877 \times 10^{-9}$	$2.62175 \times 10^{-9}$ (From [30])
$D_{W-HT9}$	$1.319 \times 10^{-9}$	$1.80726 \times 10^{-8}$ (From [31])

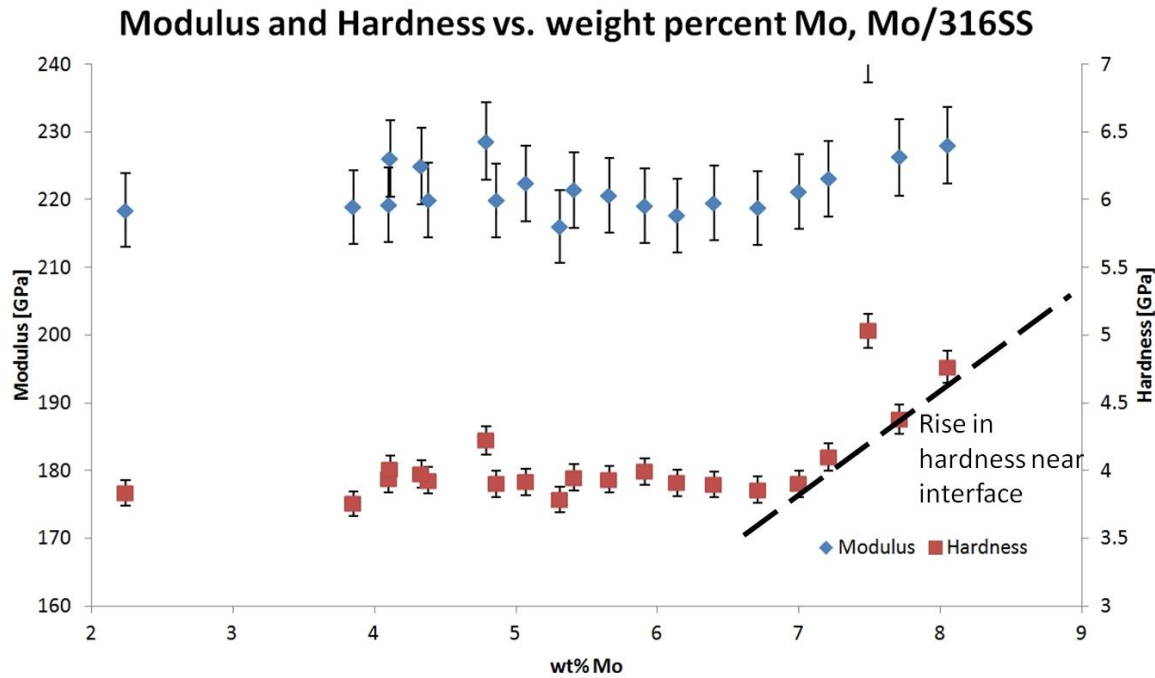
From Figure 28 and the above table, it can be concluded that the measured diffusivities are strongly dependent on the type of steel. In alloy HT9, the Mo and W had significantly higher diffusivities in the alloy 316 samples. This observation leads one to conclude that refractory elements that possess BCC crystal structures (Mo, W, Nb, Ta) tend to diffuse more rapidly through like crystal structures. Consequently, these elements display less diffusion in the FCC lattice of alloy 316SS. The measured diffusivities also indirectly indicate that alloy HT9 retained its BCC crystal structure while 316 SS retained its FCC crystal structure at 1100 °C.

Several variables may be attributed to the variance of the measured diffusivity values for the HT9 samples compared to previous literature. First, the nature of this diffusion problem in reality is quite complex since there are multiple species undergoing inter-diffusion, while the values from the literature are for simple, binary diffusion. It has been noted in the literature that diffusion of refractory elements can be cooperative and completely predicted from binary diffusion data. Second, there may have been error in determining the location of the effective “surface” in the 1-D diffusion analysis (i.e., where the dual-phase regions disappeared in the samples). TEM and/or surface etching would be needed to examine the nature of the ferritic/martensitic microstructure. Lastly,

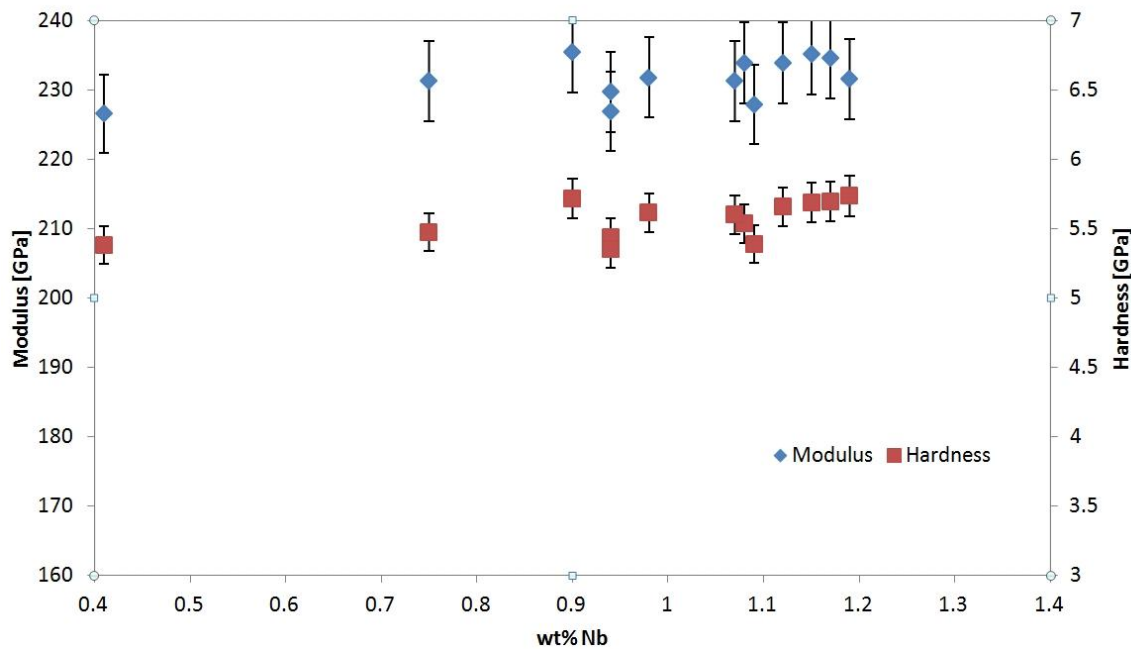
the effects of heat treatment (which thus affects microstructure) in the alloy HT9 samples may play a factor in the diffusivity of the refractory elements. A more detailed study of the diffusion kinetics would make use of multiple temperatures to try to assess the activation energies for diffusion of these elements. Additionally, using a diffusion multiple, instead of a couple, might allow for a systematic look at the role of couple diffusion between elements. Nonetheless, the initial analysis of diffusion in this thesis demonstrates basic agreement between the diffusivities of refractory elements in 316SS and in gamma iron, while the diffusivities of refractory elements in HT9 more closely resemble those observed in alpha iron.

### 3. What is the Change in Hardness, Yield Stress, and Young's Modulus with the Addition of the Refractory Element?

To illustrate the effect of each element on the mechanical properties, the results of EDS composition and nanoindentation are cross-plotted with error bars in Figures 37 and 38.



### Modulus and Hardness vs weight percent Nb, Nb/316SS



### Modulus and hardness vs. weight percent W, W/316SS

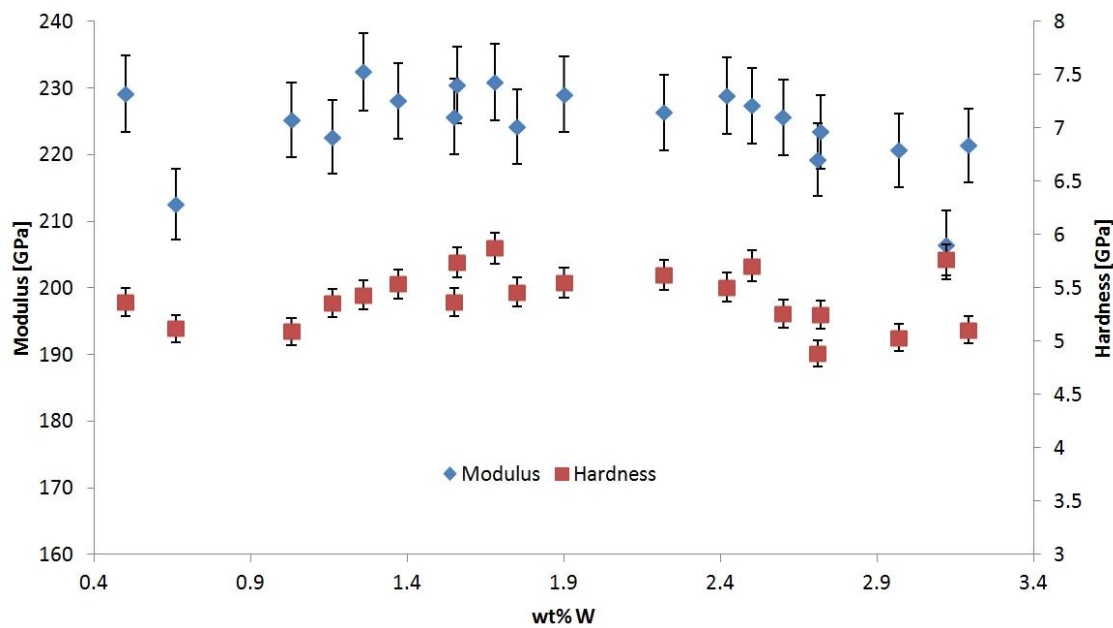
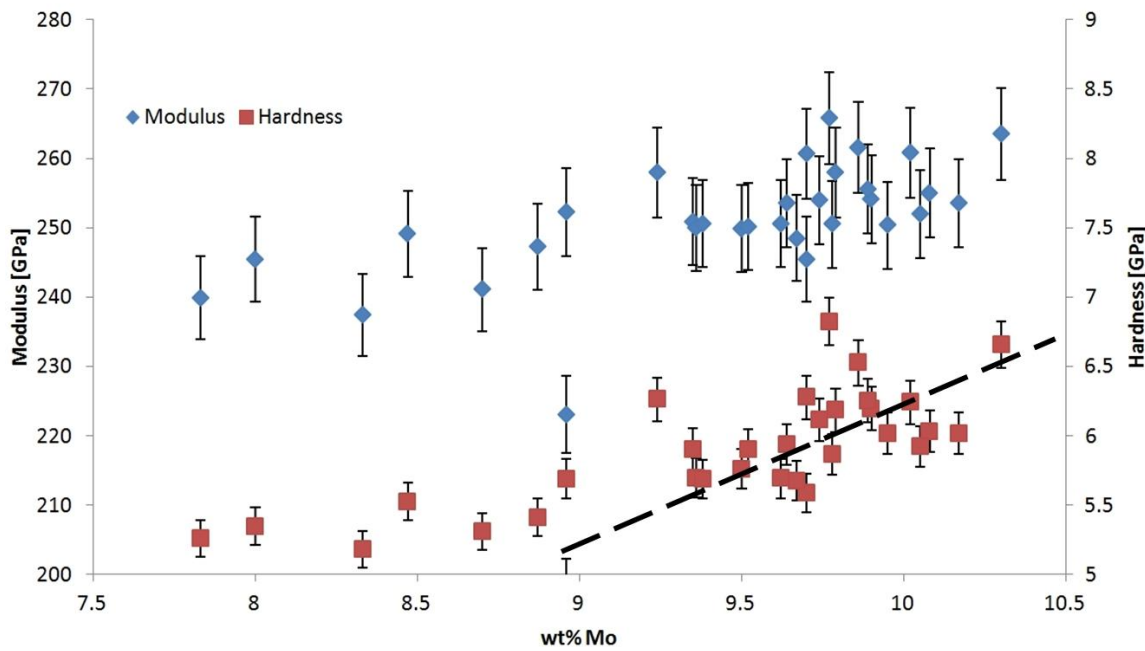


Figure 37. Graphs of modulus and hardness as a function of weight percent refractory elements in alloy 316SS. Lines added to aid the eye in trends.

### Modulus and hardness vs. weight percent Mo, Mo/HT9



### Modulus and hardness vs. weight percent W, W/HT9

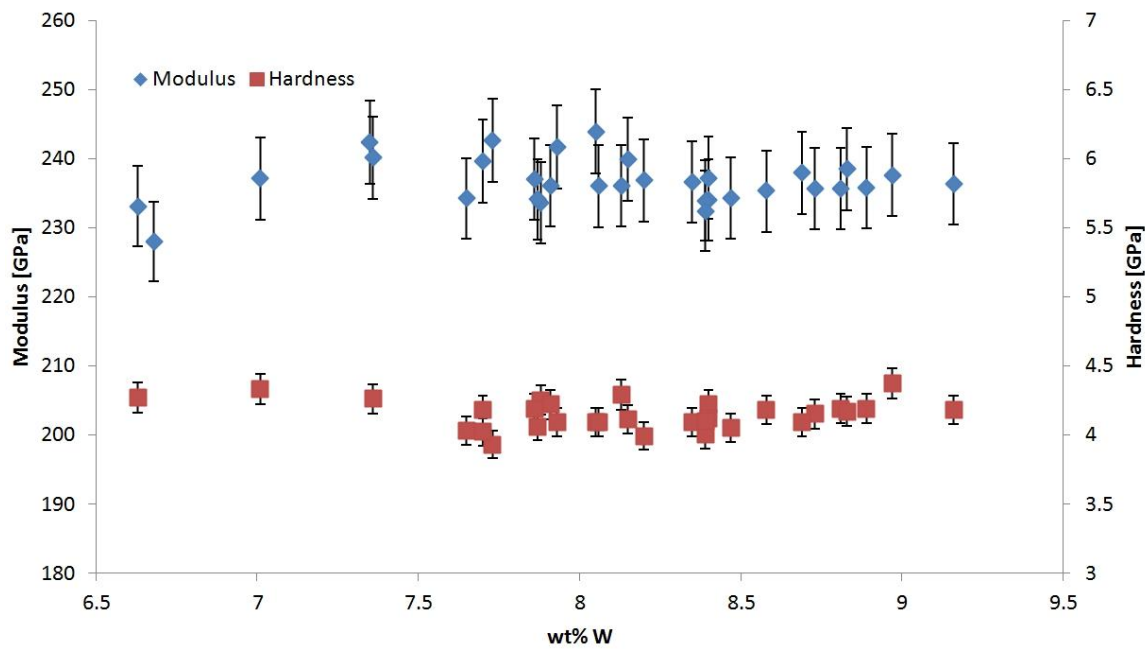


Figure 38. Graphs of modulus and hardness as a function of weight percent refractory elements in alloy HT9. Lines added to aid the eye in trends.

The molybdenum diffusion couples showed a rise in hardness with increasing concentration of refractory element, while tungsten composition showed no signs of

affecting hardness in either 316SS or HT9. The niobium diffusion couple might suggest a correlation between increased hardness and niobium content based upon the data mean trend, but this trend is not really above the noise level in the measurement. The relationship for hardness and yield stress is given by the following equation for non-work-hardened materials [17]:

$$H = 3\sigma_y \quad (5)$$

Hardness is impacted by changes both in the yield strength and work hardening rate of a metal. For materials that do not exhibit work hardening, the value  $H/3$  should yield the value of flow stress at a plastic strain of 0.375. With this caution in mind, we will estimate yield strength as being directly proportional with hardness, and estimate the change in yield stress as being  $\Delta\sigma_y = \Delta H/3$ . Using this estimate it can be suggested that the Mo and Nb samples showed a rise in yield strength with increasing refractory addition, with approximate property changes listed in Table 14. It is interesting to note that the estimated increase in yield strength for Mo-316SS and Ta-HT9 is quite large for what might be expected from solid solution strengthening alone.

Table 14. List of absolute changes in hardness, Young's Modulus, and estimated change in yield stress.

	$\Delta H$ [GPa]	$\Delta E$ [GPa]	Estimated $\Delta\sigma_y$ [MPa]
<b>Mo/316SS</b>	1	-	333.3
<b>Nb/316SS</b>	0.3	10	100
<b>Ta/316SS</b>	-	-	-
<b>W/316SS</b>	-	-	-
<b>Mo/HT9</b>	0.7	20	233.3
<b>Ta/HT9</b>	1	20	333.3
<b>W/HT9</b>	0.5	15	166.7

The assumption base on Equation 5 for estimated change in yield stress does not appear to be a realistic one. This estimate could be challenged by performing either spherical indentations, micropillar compressions, or producing micro-tensile samples at the desired refractory alloy compositions.

Given that the values of solute mismatch for Mo and W are quite close (as seen in Table 4), the fact that the addition of tungsten in solid solution did not result in a measurable change in hardness is surprising. The hypothesis that the hardening mechanism is due to solid solution strengthening from molybdenum alone is not well supported. A better hypothesis might be that the addition of Mo instead reacts with other elements, resulting precipitation hardening, e.g., formation of molybdenum carbide or nickel-molybdenum intermetallics. To answer this question would require investigation by TEM to characterize the nature of the precipitates at the nanoscale.

#### **4. Is the Diffusion Couple Approach a Useful Tool in Reactor Steel Development?**

The fabrication of the diffusion couples was successful for five of the seven samples. Intimate contact was made between the refractory elements and alloys 316SS and HT9, and three out of four elements sufficiently diffused into base metal. The fact that Ta was generally insoluble (solute size mismatch of 17.74%) and low amounts of Nb (approx. 1 wt%) were observed in the alloy 316SS (solute mismatch of 15.32%) indicates a potential shortfall in this combinatorial approach. Interestingly enough, the bond between tantalum and the steel appeared to be intact and some change in mechanical properties was observed on the steel-side of the interface; so some diffusion did take place. In order to achieve useful results with the diffusion couple method, the relative size of the solutes plays an important factor. Zirconium and hafnium, for example, would most likely be insoluble in either alloy due to their high solute mismatches (28.23% and 25% respectively). Thus, the best results obtained from this method will be when using materials with high solubility.

Materials with higher diffusivity are better candidates as well when using the diffusion couple method. This work used an initial heat treatment (i.e., heat treatment temperature and elapsed time to allow inter-diffusion of refractory elements) designed to assess the overall approach, but better results may be obtained by enabling even more diffusion by way of raising temperature and elapsed time. There is a limit to this route, however; the maximum temperature for this method will be determined by the liquidus

temperature for the alloys of interest, and the time parameter can only be increased so much until the point of thermal and chemical equilibrium is reached.

Aside from these limitations, the diffusion couple (and multiple) method when applied properly can generate vast volumes of thermodynamic, kinetic, and mechanical information of a material. It is a cost- and time-saving discipline that—when used in conjunction with traditional alloying techniques—can provide an expeditious means of identifying promising alloy combinations to accelerate the vetting process for experimental alloys.

#### **D. FUTURE WORK**

Given the success of this initial diffusion couple study, the range of compositions and temperatures should be extended. It is highly recommended that diffusion multiples be examined using multiple refractory elements within a single sample. Making several diffusion multiples at different annealing temperatures would allow better characterization of the diffusion kinetics that govern the microstructures formed in these alloys. Additionally, the parameters of the post-HIP heat treatment process (temperature and quench time) should further explored to assess their impact upon the ferritic-martensitic microstructure of the final HT-9 steel.

In order to truly understand the effects of refractory elements on the microstructural and nanoscale levels, transmission electron microscopy (TEM) is a must. Grains and grain boundaries must be examined to assess the amount of solid solutioning of refractory elements as well as carbide and precipitate formation. In the case of alloy HT9, heat treatment plays a very important role in the creation of martensite, which drives hardness, strength, ductility, and fracture toughness. Furthermore, the microstructure of the HT9 samples must be more fully investigated to evaluate the effect of the diffusion couple approach on the ferritic/martensitic microstructure of the steel.

Further evaluation of the intermetallic layers that formed between the pure, refractory metal and the steel would be useful for providing information about the phases that might be seen when precipitation and grain boundary segregation occur under neutron irradiation. Electron backscattered diffraction, or EBSD, should be applied to

these diffusion couples to catalog and assess the intermetallic phases formed during the HIP process. Nanoindentation can be used to determine the elastic modulus, hardness, and fracture toughness of these phases. The fracture toughness of these phases is particularly important as they are often responsible for crack nucleation in these alloys.

Lastly, it is highly recommended that focused ion beam (FIB) samples be cut out of the diffusion couple specimens for evaluation by TEM prior to *and* after irradiation (either ion or neutron) to evaluate the potential for refractory elements in mitigating the effects of irradiation. The performance of these alloys under irradiation was one of the original motivations for this research, and could be an important contribution to the field of alloy development for nuclear applications.

## IV. CONCLUSIONS

This thesis studied the alloying of Mo, Nb, Ta, and W refractory elements in type 316 austenitic stainless steel and HT9 ferritic/martensitic steel via the diffusion couple method. Material characterization was performed on the diffusion couple specimens via energy dispersive x-ray spectroscopy (EDS) and nanoindentation to determine thermodynamic, kinetic, and mechanical properties as a function of the addition of each refractory element. Experimental results were also used to evaluate the diffusion couple approach as a useful tool in alloy development for reactor plant applications.

An evaluation of the results for these refractory metals and alloys reveals that while the diffusion couple approach can produce large amounts of useful data in a relatively short period of time, a metallurgist must take into account the relative solute mismatch size, temperature, and time to evaluate if his/her choice of material is suitable for this high-throughput method.

As expected, the solubility of the refractory elements was inversely proportional to solute-to-solvent atomic radius mismatch. Mo and W, which had the lowest mismatch, were the most soluble, while Ta (which had the highest mismatch) had no measurable solubility in either alloy. The solubility limits of Mo and W in alloy HT9 were higher than in alloy 316SS. This difference in solubility is most likely due to the presence of Ni in the stainless steel which had a suppressive effect by maintaining the austenite crystal structure at the annealing temperature. The solubilities of the refractory elements are consistent with the ternary phase diagrams of the refractory element, Fe, and Cr at 1100 °C.

The measured diffusivities of the refractory elements in the steels were strongly dependent upon the crystal structure of the base steel. Diffusivity of Mo and W in alloy HT9 (an  $\alpha$ -Fe solid solution) was two orders of magnitude higher than that of alloy 316SS (a  $\gamma$ -Fe solid solution). The higher diffusivity can be justified by the fact that both alloy HT9 and the refractory elements both possess a BCC crystal structure.

Nanoindentation revealed a positive correlation between hardness as a function of composition of Mo and Nb in the steels, but no hardening effect with the addition of W in either alloy 316SS or HT9 was observed. It can be postulated that the effect on mechanical properties in Mo is due to precipitation hardening vice solid solution strengthening. The exact mechanism of hardening is not known at this time.

## LIST OF REFERENCES

- [1] G. S. Was and P. L. Andresen, “Stress corrosion cracking behavior of alloys in aggressive nuclear reactor core environments,” *NACE International*, 2005, vol. 63, no. 1, 2007.
- [2] D. Olander, *Fundamental Aspects of Nuclear Reactor Fuel Elements: 001 (Tid 26711 P1)*. Springfield: Us Dept of Energy, 1976.
- [3] E. A. Little, “Development of radiation resistant materials for advanced nuclear power plant,” *Materials Science*, no. May, 2006.
- [4] N. Hashimoto, J. P. Robertson, and K. Shiba, “Microstructure of isotropically-tailored martensitic Steel HT9 irradiated at 400C to 7 dpa in HFIR,” *Oak Ridge National Laboratory*, vol. 2, pp. 96–101.
- [5] J. Gan, E. Simonen, S. Bruemmer, L. Fournier, B. Sencer, and G. Was, “The effect of oversized solute additions on the microstructure of 316SS irradiated with 5 MeV Ni++ ions or 3.2 MeV protons,” *Journal of Nuclear Materials*, vol. 325, no. 2–3, pp. 94–106, Feb. 2004.
- [6] K. Nakata, S. Kasahara, and H. Takahashi, “Effect of Mn addition on decrease of Cr depletion at grain boundary in austenitic alloys irradiated with electrons,” *Science*, vol. 239, pp. 194–199, 1996.
- [7] R. L. Klueh, “ELEVATED-TEMPERATURE FERRITIC AND MARTENSITIC STEELS AND THEIR APPLICATION TO FUTURE,” *Oak Ridge National Laboratory*, no. November, 2004.
- [8] M. Victoria, N. Baluc, C. Bailat, Y. Dai, M. I. Lippo, and R. Sch, “The microstructure and associated tensile properties of irradiated fcc and bcc metals,” *Journal of Nuclear Materials*, vol. 276, pp. 114–122, 2000.
- [9] A. Jenssen, L. G. Ljungberg, J. Walmsey, and S. Fisher, “Importance of molybdenum on irradiation-assisted stress corrosion cracking in austenitic stainless steels,” *NACE International*, 1998, vol. 96, 1998.
- [10] H. M. Chung, “Assessment of void swelling in austenitic stainless steel core internals assessment of void swelling in austenitic stainless steel core internals,” U.S. Nuclear Regulatory Commission, Washington, D.C., 2006.
- [11] E. H. Lee, T. S. Byun, J. D. Hunn, K. Farrell, and L. K. Mansur, “Origin of hardening and deformation mechanisms in irradiated 316 LN austenitic stainless steel,” *Journal of Nuclear Materials*, vol. 296, no. 2001, pp. 183–191, 2008.

- [12] R. L. Klueh and A. T. Nelson, “Ferritic/martensitic steels for next-generation reactors,” *Journal of Nuclear Materials*, vol. 371, no. 1–3, pp. 37–52, Sep. 2007.
- [13] N. E. Todreas and M. Kazimi, *Nuclear Systems Volume I: Thermal Hydraulic Fundamentals*. Taylor & Francis.
- [14] B. Leffler, “Stainless steels and their properties,” *Welding Journal*, vol. I, pp. 1–45, 2000.
- [15] S. J. Zinkle and N. M. Ghoniemb, “Operating temperature windows for fusion reactor structural materials,” vol. 52, no. 2000, pp. 55–71, 2008.
- [16] R. L. Klueh and D. R. Harries, *High-Chromium Ferritic and Martensitic Steels for Nuclear Applications: Monograph 3 (Monograph (American Society for Testing and Materials), 3.)*. West Conshocken: American Society for Testing & Materials, 2001.
- [17] M. A. Meyers and K. K. Chawla, *Mechanical Behavior of Materials*, 2nd ed. Cambridge: Cambridge University Press, 2009.
- [18] W. D. Callister, *Materials Science and Engineering: An Introduction*, 8th ed. John Wiley & Sons, 2010.
- [19] M. J. Hackett, J. T. Busby, M. K. Miller, and G. S. Was, “Effects of oversized solutes on radiation-induced segregation in austenitic stainless steels,” *Journal of Nuclear Materials*, vol. 389, no. 2, pp. 265–278, May 2009.
- [20] R. A. Potyrailo and E. J. Amis, *High-Throughput Analysis: A Tool for Combinatorial Materials Science*. New York: Springer, 2003.
- [21] J.-C. Zhao, “The diffusion-multiple approach to designing alloys,” *Annual Review of Materials Research*, vol. 35, no. 1, pp. 51–73, Aug. 2005.
- [22] J. I. Goldstein, D. E. Newbury, P. Echlin, and D. C. Joy, *Scanning Electron Microscopy and X-ray Microanalysis: A Text for Biologists, Materials Scientists and Geologists*, 2nd ed. New York: Kluwer Academic / Plenum Publishers, 1992.
- [23] D. A. Porter and K. E. Easterling, *Phase Transformations in Metals and Alloys*. Berkshire: Van Nost. Reinhold, U.S., 1981.
- [24] “Agilent Technologies G200 Nano Indenter User’s Guide.” Agilent Technologies, Inc., Chandler, AZ, 2009.
- [25] J. Hay, P. Agee, and E. Herbert, “Continuous stiffness measurement during instrumented indentation testing,” *Experimental Techniques*, vol. 34, no. 3, pp. 86–94, Jan. 2010.

- [26] P. Villars, H. Okamoto, and K. Cenzual, “ASM Alloy Phase Diagrams Center,” 2006. [Online]. Available: <http://www1.asminternational.org/AsmEnterprise/APD>.
- [27] R. V. Patil, G. P. Tiwari, and B. D. Sharma, “Patil\_Mo diffusion in 316 SS,” *Metal Science*, vol. 14, no. 11, pp. 525–528, 1980.
- [28] A. Shaikh, “Interdiffusion measurement of niobium and tantalum in iron base alloys,” *Materials Science and Technology*, vol. 6, no. December, 1990.
- [29] I. K. Kupalova and S. V. Zemskii, “Diffusion of tungsten in austenite in high-speed steels,” *Metal Science and Heat Treatment*, vol. 10, no. 2, pp. 93–95, 1968.
- [30] N. Oono, H. Nitta, and Y. Iijima, “Diffusion of niobium in  $\alpha$ -iron,” *Science*, vol. 44, no. 10, pp. 2078–2083, 2003.
- [31] S. Takemoto, H. Nitta, Y. Iijima, and Y. Yamazaki, “Diffusion of tungsten in  $\alpha$ -iron,” *Philosophical Magazine*, vol. 87, no. 11, pp. 1619–1629, Apr. 2007.

THIS PAGE INTENTIONALLY LEFT BLANK

## **INITIAL DISTRIBUTION LIST**

1. Defense Technical Information Center  
Ft. Belvoir, Virginia
2. Dudley Knox Library  
Naval Postgraduate School  
Monterey, California
3. MAE Department Chairman,  
Dr. Knox Millsaps  
Naval Postgraduate School  
Monterey, California
4. Engineering and Technology Curricular Office, Code 34  
Naval Postgraduate School  
Monterey, California
5. Professor Luke N. Brewer  
Naval Postgraduate School  
Monterey, California
6. Professor Sarath Menon  
Naval Postgraduate School  
Monterey, California